DOCTORATE THESIS

Dynamics of particles in fluids: effects of correlations and interactions

ANSHUMAN DUBEY

Department of Physics
University of Gothenburg
Göteborg, Sweden 2022

Dynamics of particles in fluids: effects of correlations and interactions
Anshuman Dubey

ISBN 978-91-8009-662-1 (PRINT)
ISBN 978-91-8009-663-8 (PDF)

This thesis is electronically published, available at
http://hdl.handle.net/2077/70250

Department of Physics
University of Gothenburg
SE-412 96 Göteborg
Sweden
Telephone: +46 (0)31-786 00 00

Front cover: Probability of separations, $P(\boldsymbol{R})$, on a Logarithmic colour scale for non-dimensional settling parameter $Q = 8.1$ and radius ratio $a_1/a_2 = 0.9$, see Paper D and Chapter 9.

Printed by Stema Specialtryck AB
Göteborg, Sweden 2022

ABSTRACT

Particles suspended in turbulent fluid flows are common in Nature and in technological applications. In some cases, the relative dynamics of spherical particles may be of interest. One example is small rain droplets in turbulent clouds. The dynamics of nearby droplets is correlated because they experience a correlated airflow. But their relative dynamics is influenced also by fluid-mediated droplet-droplet interactions, or by electrical forces due to charges which the droplets may carry. Heavy particles may detach from the fluid streamlines due to inertia and show inhomogeneities in their spatial distributions, known as clustering. In other cases, the angular dynamics of aspherical particles may be of interest, an example being long and slender fibres in wood pulp used for papermaking. In this thesis, we start by studying the separations and relative angles of non-interacting particles in turbulent flows. This is followed by two studies on the relative dynamics of interacting droplets in steady flows.

First, we analyse a discrete-time, toy model of inertial particles in turbulence. The simplicity of the model allows us to understand in detail how the distribution of inertial particles in turbulence depends on the particle inertia.

Second, we use a statistical model to study how slender rods align with the Lagrangian stretching direction in a turbulent channel flow. We show that the alignment is stronger near the channel wall, than near the channel center. Nevertheless, the rods show large excursions away from alignment. Our model explains the dynamics qualitatively near the channel center but quantitatively near the channel wall.

Third, we use dynamical systems theory to unravel the mechanisms leading to collisions of small, charged droplets in still air. We find that a saddle point with its associated stable manifold determines whether droplets collide or not. This mechanism causes the collision outcomes of droplets with large charges to become independent of non-continuum effects.

Finally, we perform a bifurcation analysis of hydrodynamically interacting neutral droplets settling in a straining flow. Our analysis explains a non-monotonic dependence of their collision rate upon the strength of the strain and that of gravity. We find that even for neutral droplets, there is a regime where the steady-state collision rate becomes independent of non-continuum effects. In addition, our analysis predicts strong inhomogeneities in the distribution of separations.

List of papers

This thesis consists of an introductory text and the following four appended papers:

Paper A

Dubey, A., Meibohm, J., Gustavsson, K., & Mehlig, B. 2018 Fractal dimensions and trajectory crossings in correlated random walks. *Physical Review E* **98** (6), 062117.

Paper B

Cui, Z., Dubey, A., Zhao, L., & Mehlig, B. 2020 Alignment statistics of rods with the Lagrangian stretching direction in a channel flow. *Journal of Fluid Mechanics,* **901***, A16.*

Paper C

Magnusson, G., Dubey, A., Kearney, R., Bewley, G.P., & Mehlig, B. 2021 Collisions of micron-sized, charged water droplets in still air. *arXiv e-print 2106.11543*

Paper D

Dubey, A., Gustavsson, K., Bewley, G.P., & Mehlig, B. 2022 Bifurcations in droplet collisions. *In review*

My contributions

My contributions to the appended publications are:

Paper A

I performed the computation of the correlation dimension. JM and I wrote the paper together, with help of BM.

Paper B

I performed the data analysis and all analytical calculations. I developed the theory, with help from BM. I wrote the paper with help from BM.

Paper C

I took part in the data analysis. I devised the model and developed the theory with help from BM. I performed all analytical calculations, numerical simulations, and fits to the experimental data. I contributed to the writing of the main paper. I wrote the Appendix, with the exception of Sections I and II.

Paper D

I suggested to perform a bifurcation analysis for neutral droplets in steady flows. I implemented the numerical simulations and computed the analytical results. BM and I developed the theory together. I contributed to the writing of the paper.

CONTENTS

PART I
INTRODUCTION

Particles in fluid flows are present all around us. One example is water droplets in clouds [1]. A second example is slender fibres in wood pulp used in the papermaking industry [2]. Fluid flows in such systems are usually in a state of complicated, chaotic motion, called turbulence [3]. Turbulent flows exhibit velocities and pressures which fluctuate both in space and in time. Two particles which are close to each other in such a flow can become correlated because they experience approximately the same flow. Due to their correlated motion and because the dynamics are dissipative due to viscous friction [4, 5], the particles phase-space volume contracts over time and they exhibit clustering [6]. Clustering is characterised by divergent spatial densities in particle distributions, and can enhance the rate at which particles collide [7, 8].

Yet, if the particles approach very close, they begin to interact directly, through charges which they might carry [9], but also through the surrounding fluid [10, 11]. How interactions affect the rate at which droplets in air collide with each other has been a subject of active research in the past 70 years [12, 13]. Hydrodynamic interactions tend to bend one particle's trajectory around the other [14]. From this one might expect that hydrodynamic interactions prevent droplets from approaching each other. Yet, recent experimental observations of the relative dynamics of particles in air exhibit large distributions of separations and remain unexplained by current theories [15].

In this thesis we use simple models to understand the dynamics of particles in flows. The questions considered in this thesis concern two aspects. First, the correlated motion of non-interacting inertial particles, as well as the angular dynamics on non-inertial rods is studied. In these cases the focus is on describing the distributions of particle positions and angles. Second, the relative dynamics of interacting spherical particles is studied: the effects of electrical charges as well as fluid-mediated interactions are considered. In these cases, the focus changes towards understanding collision dynamics of interacting droplets.

Structure of this thesis

This thesis consists of a text forming a frame for the appended papers. Part I, forms an introductory text which motivates our research. This is followed by a layman's introduction aimed at an undergraduate student or even a curious highschool student, with the hope that an expert would find it informative as well. Part II compiles the technical background required to understand this thesis. Part III consists of backgrounds of the individual problems considered, main results, and in some cases more detailed discussions of the contents of the appended research papers. Part IV is the Appendix and Part V consists of reprints of the appended paper A – D.

1 Motivation

The dynamics of non-interacting particles in turbulent flows has a long history [6, 16]. One of the first steps was a theoretical model explaining how turbulent strains increase the collision rate of droplets, ignoring any hydrodynamic interaction [17]. Furthermore, this study ignored the effect of particle inertia on the droplet dynamics. It was therefore valid for tracer particles advected by the fluid.

But is it appropriate to ignore the inertia of the particles? After all, the behaviour of inertial particles in a fluid-flow is qualitatively different from that of tracer particles. While tracer particles tend to follow the streamlines of the advecting fluid, inertial particles may detach from them. This detachment from fluid streamlines has important consequences [6]. First, it allows the particle trajectories to cross at non-zero relative velocities leading to divergences in the spatial distributions of particles [6, 7]. Second, it causes particles to deplete from regions of high vorticity and accumulate in regions of large strains [8, 18].

The mechanisms outlined above indicate that inertia causes large, or even divergent spatial densities to appear in distributions of particles in turbulence, a phenomenon called clustering [6, 19]. On the other hand, clustering directly implies that large regions in space are devoid of particles. In fact, particles in turbulence are distributed on sets with interesting properties [20, 21, 22]. They do not fill out the complete volume of the space they inhabit, yet, neither do they collapse on a point, or a line, or a surface. These sets are instead

somewhere in between, and are known as fractals [4, 23]. It is important to quantify the properties of these fractals because one consequence of particles distributing on fractal sets can be high probabilities of finding two particles close together [6]. This could in turn increase their collision rates [16].

Despite accounting for particle inertia, the studies mentioned above ignore how the fluid-mediated droplet-droplet interactions [10, 11] affect the particle dynamics. This is a logical first step because firstly, the non-interacting approximation discussed above is valid as long as the particles are farther apart than a few particle radii. In that regime, the relative velocities and distribution of separations of particles must be described by the models used in the studies described above. Secondly, the experimental and numerical complexities involved have proved it challenging to accurately study the particle dynamics while accounting for droplet-droplet interactions [13].

Until very recently [15, 24], lack of high-resolution techniques have proved it impossible to perform experimental observations of the relative dynamics of droplets. On the other hand, solving this task computationally is challenging because solving the fluid equations and simultaneously computing the force on particles requires large amount of computing power [25]. The computing power required increases both as the number of particles increases and as the turbulence intensity increases.

In order to circumvent the problems with experiments and direct numerical simulations discussed above, model simulations have been widely employed in the past decades [13]. The simplest model of hydrodynamic interactions computes how the relative dynamics of particles changes at large separation in a slowly flowing fluid, the so called creeping-flow approximation [11]. While this model may be extended to describe the relative dynamics at any value of particle separation [26], the studies summarised in Ref. [13] approximate these forces using ad-hoc schemes whose validity is hard to justify. Most importantly, they fail to explain the distributions of relative separations observed in recent experiments or illuminate the mechanisms which may give rise to them [15].

In addition to hydrodynamic interactions, droplets in clouds carry electrical charges [9] and may interact through electrical forces. Several studies have considered the effect of droplet charges on the dynamics of settling droplets [27, 28, 29]. They found that collision efficiencies increase with increasing charge. Yet, these studies either ignore hydrodynamic interactions altogether or only consider hydrodynamic interaction for widely separated droplets. How

these approximations fail outside their regime of validity is not considered.

Finally, in some cases the angular dynamics of particles may be of interest. For instance, wood pulp consisting of slender wood fibres is used to make paper [2]. Fibres aligned in the same direction result in good quality paper. More fundamentally, two nearby slender rods in a turbulent flow typically align well with each other, but sometimes show large deviations away from alignment [30]. Which mechanisms give rise to these large excursions is not known.

In this thesis we start by considering the dynamics of non-interacting particles, which are nevertheless correlated through the fluid flow they experience. In paper A we use a simple discrete-time, toy model of inertial particles in a random flow to quantify how the particle distribution changes as the inertia parameter is varied. In paper B we analyse the angular dynamics of slender rods in a turbulent channel flow, an example of a turbulent flow with boundaries. Next, we consider the effect of interactions. In paper C we describe the collision dynamics of hydrodynamically-interacting, charged water droplets settling in quiescent air using dynamical systems theory. Finally, in paper D we explain the collision dynamics of neutral droplets which interact hydrodynamically at interfacial separations larger than the mean-free-path of air. But when this separation becomes comparable to the mean-free-path of air, non-continuum forces between the droplets dictate their relative dynamics.

2 A layman's introduction

In this chapter I give an introduction to the subject of particles in fluid flows. This chapter is meant to introduce the subject not to an expert, but rather to an undergraduate student, or perhaps even a particularly curious high-school student. The focus is on qualitatively describing a system consisting of particles in flows in terms of dimensionless numbers.

Fluid dynamics

In order to describe the dynamic motion of particles in flows, we must understand basic properties of the fluid flow itself. In Nature, Fluid flow arises due to the motion of many small molecules: water consists of water molecules,

air is a mixture of various different gases like oxygen and nitrogen. However, when dynamics occurs at length scales much larger than the mean-free-path of air, the description becomes much simpler: what we observe every day as a fluid. One important aspect of fluids is the fluid viscosity. Fluid viscosity refers to the propensity of the fluid to resist relative motion between two layers of the fluid. Viscosity quantifies in a sense the internal friction of the fluid to its own flow. For example, honey is more viscous than water. When using a spoon to drizzle honey it flows in a slow and sluggish manner due to high viscosity. Water on the other hand can be easily poured from a spoon due to low viscosity.

Rigid particles

We model particles as rigid bodies. Rigid bodies are defined as objects that either do not deform or deform so little that the deformation is negligible. In the case of solids, it is the strong inter-molecular forces preventing the solid from deforming, competing with the relatively weak fluid stress at the particle surface, and so rigid particles are a good approximation. For water droplets in air, the surface tension attempts to keeps the droplet spherical while the stress at the droplet surface tries to deform it. When the droplets are small, the surface tension is strong and thus the droplets remain spherical.

The combined fluid-particle system

Solving a coupled fluid-particle system is a hard problem because the presence of the particle disturbs the flow and this new flow in turn affects the particle differently compared to the original flow. However, the disturbance that the particle causes in the flow must be in some way related to the size of the particle: the larger the particle, the larger the disturbance. In fact, when the particles are small the motion of the particle in the fluid is not affected by this disturbance. How small the particle needs to be requires dimensionless numbers and is discussed in the next section. In a system consisting of a fluid and many particles its possible that the particles interact directly, say by colliding or by electric forces. Another possibility is that the wake of one particle affects another particle. But when the particle number density is small or the particle separation is large, these effects can be neglected.

Dimensionless numbers

Dimensionless numbers allow us to compare things, and usually reduce the number of parameter in the problem. For example, consider a plastic ball and a metal ball in water. The plastic ball floats and the metal ball sinks. In contrast, in air, both the plastic and metal balls sink. From this one would conclude that the density of the ball as well as the density of the fluid are important. In fact, due to Archimedes we know that it is only the dimensionless ratio of the two densities which is important, thus the problem is reduced from two dimensionful parameters to one dimensionless parameter. In this Section we introduce six dimensionless numbers important for the problems discussed in this thesis.

Stokes number

The Stokes number is a measure of the inertia of a particle in a flow. Particle inertia can be imagined as the particle's reluctance to respond to a force, in our case the force is due to friction with the fluid at the particles surface. This reluctance of the particle in the flow sets a time scale τ_p, the particle relaxation time, related to particle dynamics. At the same time the flow itself fluctuates with some characteristic time scale. The ratio of these two time scales defines the Stokes number, St. Thus the Stokes number measures how well a particle responds to changes in fluid velocity. A very small Stokes number corresponds to particles that essentially change velocity very quickly when the fluid velocity changes. On the other hand a very large Stokes number corresponds to particles that behave like bullets and do not change direction regardless of a change in the fluid velocity.

Kubo number

The Kubo number is a dimensionless number associated to a flow, and measures how persistent the flow is. Observe a flow at a fixed point in space. In a gentle stream the flow at a fixed point might remain the same for a long time. In contrast, in an energetic waterfall, the flow at any point changes quickly. This defines a time scale called the correlation time of the flow. A second time scale related to the flow can be formed by dividing the correlation length of the flow by the magnitude of the flow velocity fluctuations. This is the so-

called advection time of the flow, named so because it is the time an advected fluid parcel needs to travel one correlation length. Comparing the fluctuation time of the flow to this advection time forms another dimensionless number called the Kubo number, Ku.

Particle Reynolds number

The particle Reynolds number is a measure of the importance of fluid inertia for particle dynamics. When a particle immersed in a fluid moves, the fluid layers adjacent to it will stick to the particle and move along with it. But the layers farther away will resist the motion due to their inertia. The faster a particle moves, the thinner a layer is able to stick to the particle because by the time the fluid with its inertia can respond, the particle has already moved. This thickness of fluid that sticks to the particle defines the viscous length scale. The particle Reynolds number is defined as the ratio of particle size to the viscous length scale. Thus a particle much smaller than the viscous length scale simply sees a viscous flow, without worrying about fluid inertial effects.

Strouhal number

The Strouhal number is a dimensionless parameter which compares the timescale at which the particle accelerates to the timescale at which the fluid accelerates. If a particle travelling in a fluid accelerates very slowly, the fluid around it moves in a quasi-steady manner. This means that the fluid velocity can relax to its quasi-steady value quickly and the time dependent term in the Stokes (or Navier-Stokes) equation can be ignored. By contrast, if the particle accelerates rapidly, the fluid surrounding it is accelerated as well. The quasi-steady approximation is no longer valid. The ratio of timescale of acceleration of the particle to the timescale of acceleration of the fluid forms the dimensionless number, the Strouhal number, quantifying the importance of unsteadiness.

Knudsen number

A hydrodynamic description of air is valid at length scales much larger than the mean free path of molecules in air. However, when the length scales of interest, such as the distance between the surfaces of two water drops in air, becomes comparable to the mean free path of air, the hydrodynamic

approximation must fail. The importance of this breakdown of the continuum approximation is quantified by the ratio of the mean free path of air to the radius of a droplet.

Coulomb number

The Coulomb number is a measure of the the importance of charges compared to the relative velocity of two droplets. It is defined as the ratio of the Coulomb potential energy upon contact, to the initial relative kinetic energy of the droplets. A small Coulomb number corresponds to weak charges, while a large Coulomb number corresponds to strong charges.

Part II
Background

3 Fluid flows

The description of particles in a flowing or steady fluid must necessarily refer to the underlying flow. In this thesis, we are interested in flows which model turbulent flows (used in papers A and B) but also quiescent fluids (paper C) and steady flows (paper D).

In order to model turbulent flows sufficiently well so that their effects on particle dynamics can be reproduced, it is useful to discuss some aspects of turbulent flows. The Navier-Stokes equations are expected to contain all aspects of turbulent flows observed in Nature [3]. These equations and some characteristic aspects of its solutions far from any boundaries are discussed in Section 3.1. Yet, not all flows of interest occur far from boundaries. How the presence of a boundary affects turbulent flows is important in industrial applications, one example is papermaking [2]. A simple model for wall-bounded turbulent flows is a turbulent channel flow. This is the subject of Section 3.2.

One way to approach the problem of understanding the dynamics of particles in turbulent flows is to numerically solve the Navier-Stokes equations and use an effective equation of motion to integrate particle trajectories [31]. This approach, while immensely successful, first, does not immediately illuminate the physical mechanisms leading to an observed phenomenon, and second, the control over physical parameters such as length and timescales of the flow is limited by computational cost. These problems may be circumvented by using synthetic, random flow fields which reproduce some but by no means all properties of turbulent flows [6]. These random flows provide full control over the length and timescale characterising the flow. This control over the timescales, in particular, allows to approach the white-noise limit which might be analytically tractable through the Fokker-Planck equation [32]. We introduce a synthetic, Gaussian flow in Section 3.3.

3.1 Navier-Stokes equations

In this Section I discuss the Navier-Stokes equations, and turbulence. A discussion of two important quantities of the fluid flow, the velocity-gradient and the left Cauchy-Green tensor follows. The fluid velocity-gradient will be crucial for the angular dynamics of small rods. The left Cauchy-Green tensor

describes how small fluid volumes stretch and rotate and thus can be used to define a reference frame unique to flow streamlines. The leading eigenvector of the left Cauchy-Green tensor was first used in Ref. [33] followed by Ref. [34] to study alignment of rods in two-dimensional flows. The left Cauchy-Green tensor will be important in studying alignment of slender rods in Chapter 7.

The discussion of the Navier-Stokes equations and turbulence in this section closely follows Ref. [3]. The incompressible Navier-Stokes equations describe how the fluid velocity $\boldsymbol{u}$ at a given position changes with time. The equations read [3],

$$\partial_t \boldsymbol{u} + \boldsymbol{u} \cdot \nabla \boldsymbol{u} = -\frac{1}{\rho_\mathrm{f}} \nabla p + \nu_\mathrm{f} \nabla^2 \boldsymbol{u} + \boldsymbol{F}, \tag{3.1}$$

$$\nabla \cdot \boldsymbol{u} = 0. \tag{3.2}$$

Here p is the fluid pressure, ν_f its kinematic viscosity and ρ_f its mass-density. $\boldsymbol{F}$ is a forcing term which injects energy at large scales at a constant rate $\varepsilon = \langle \boldsymbol{F} \cdot \boldsymbol{u} \rangle$. ∇ denotes the gradient, and ∇^2 the Laplacian operator. Note that the position dependence of the velocity and pressure is suppressed in Eqs. (3.1)-(3.2). We dedimensionalize the Navier-Stokes equation as follows:

$$\boldsymbol{x} \to L_0 \boldsymbol{x}\,, \tag{3.3}$$

$$\boldsymbol{u} \to U_0 \boldsymbol{u}\,, \tag{3.4}$$

$$p \to \frac{\nu_\mathrm{f} \rho_\mathrm{f} U_0}{L_0} p\,, \tag{3.5}$$

$$\boldsymbol{F} \to \frac{\nu_\mathrm{f} U_0}{L_0^2} \boldsymbol{F}\,. \tag{3.6}$$

Here U_0 and L_0 correspond to large scale velocity and length scales. This gives the dedimensionalized equations,

$$\mathrm{Re}(\partial_t \boldsymbol{u} + \boldsymbol{u} \cdot \nabla \boldsymbol{u}) = -\nabla p + \nabla^2 \boldsymbol{u} + \boldsymbol{F}, \tag{3.7}$$

$$\nabla \cdot \boldsymbol{u} = 0. \tag{3.8}$$

The dimensionless number Re is called the Reynolds number based on the integral length and velocity scales, L_0 and U_0. Note that this Reynolds number was not discussed in the Chapter 2. The Reynolds number depends on the length scale L_0 and velocity scale U_0 of the system, and the viscosity μ and

mass-density ρ_f of the fluid as follows,

$$\mathrm{Re} = \frac{\rho_f U_0^2/L_0}{\mu U_0/L_0^2} = \frac{L_0 U_0}{\nu_f}. \tag{3.9}$$

Here $\mu = \nu_f \rho_f$ is called the dynamic viscosity of the fluid. The quantity $\mu U_0/L_0^2$ is the typical magnitude of viscous terms in the Navier-Stokes equations: the terms on the right-hand side of Eq. (3.1). While $\rho_f U_0^2/L_0$ is the typical magnitude of inertial terms, the terms on the left-hand side of Eq. (3.1). Thus the Reynolds number determines the relative magnitude of fluid inertial effects compared to viscous effects. This is important because the two effects lead to qualitatively different solutions of the Navier-Stokes equations.

A purely viscous flow is obtained at $\mathrm{Re} = 0$. This leads to the Stokes equations [11], which read,

$$-\nabla p + \nabla^2 \boldsymbol{u} + \boldsymbol{F} = 0, \tag{3.10}$$

$$\nabla \cdot \boldsymbol{u} = 0. \tag{3.11}$$

Solutions to the Stokes equations, called Stokes flows depend only on the geometry of the container and the boundary conditions. Stokes flows describe purely viscous flows. Viscosity qualitatively corresponds to friction between fluid layers and thus leads to dissipation and loss of energy. Dissipation is also the reason for having the forcing term, $\boldsymbol{F}$, in both the Stokes and Navier-Stokes equations. Without the forcing term, or flowing boundary conditions at infinity, the equations dissipate all energy injected initially and the fluid stops flowing.

At large Reynolds numbers, $\mathrm{Re} \gg 1$, fluids exhibit chaotic motion. Turbulence does not have a well defined mathematical definition but may be recognised by its characteristics, one of them being chaotic motion, while others are discussed below. One way to visualise turbulence is by considering what happens to nearby fluid particles. As time evolves, two fluid particles which start close together separate rapidly from each other, on average. This in turn leads to quick intermixing of the fluid.

Fully developed turbulence consists of eddies of a vast range of sizes. The largest eddies have sizes comparable to the forcing scale L_0. These large eddies themselves drive smaller eddies, which in turn drive even smaller eddies. In this way, the energy injected at large scales cascades down to

smaller scales. This process does not continue indefinitely, but stops when the smallest eddies with sizes comparable to the Kolmogorov length scale, $\eta_K = (\frac{\nu_f^3}{\varepsilon})^{1/4}$ dissipate their energy due to viscous friction.

A third feature of turbulence is the sweeping of smaller eddies by larger ones. This is a consequence of the self-advecting nature of the velocity field due to the $\boldsymbol{u} \cdot \nabla \boldsymbol{u}$ term in Eq. (3.7). And lastly, the spatial gradients of turbulent velocity fields can exhibit large deviations away from their mean values [35].

At this point a relevant question is how is the Reynolds number relevant for everyday life? It turns out that large Reynolds number flows are commonly encountered. This is due to the small kinematic viscosity of water and air, roughly of the order of $10^{-6} - 10^{-5}$ m^2/sec. Even a small gust with wind velocity of a few m/s over a length of a few meters easily reaches large Reynolds numbers of the order of $10^4 - 10^5$. Thus, high Reynolds number turbulent flows are more the norm than the exception.

In summary, the intensity of turbulent flows is determined by its average energy dissipation rate per unit mass, usually denoted ε, with units m^2/s^3. Turbulent flows exhibit several universal small-scale features which are important for particles in turbulence. The first is a length scale, called the Kolmogorov length, defined above. Second, the Kolmogorov time scale is defined as $\tau_K = \sqrt{\frac{\nu_f}{\varepsilon}}$. This is the smallest timescale at which the fluid velocity fluctuates.

Fluid velocity-gradient tensor

The spatial gradients of fluid velocity define how different is the velocity at two points very close together. The fluid velocity-gradient tensor $\mathbb{A}$ reads,

$$A_{ij} = \frac{\partial u_i}{\partial x_j}. \tag{3.12}$$

This velocity-gradient tensor can be decomposed into its symmetric part $\mathbb{S}$, and anti-symmetric part $\mathbb{O}$ as follows:

$$\mathbb{S} = \frac{1}{2}(\mathbb{A} + \mathbb{A}^\intercal), \tag{3.13}$$

$$\mathbb{O} = \frac{1}{2}(\mathbb{A} - \mathbb{A}^\intercal). \tag{3.14}$$

Here S is called the strain-rate matrix and quantifies the rate-of-strain of the fluid flow. The vorticity $\mathbb{O}$ quantifies the rotation associated to the flow field $\boldsymbol{u}$.

The strain tends to deform infinitesimal volumes of the fluid. The vorticity, on the other hand, simply rotates an infinitesimal volume of fluid around an axis defined by the vorticity vector ω,

$$\boldsymbol{\omega} = \nabla \times \boldsymbol{u}. \tag{3.15}$$

The vorticity vector can be expressed in index notation: $\omega_i = 2\varepsilon_{ijk}O_{jk}$, where ε_{ijk} is Levi-Civita tensor and repeated indices indicate the Einstein summation convention. The magnitude of the vorticity vector, $|\boldsymbol{\omega}|$, gives the angular velocity of rotation.

Lagrangian stretching direction

A fluid parcel advected by a fluid flow deforms and rotates due to the fluid vorticity and strain. This effect can be described by following a tracer particle at $\boldsymbol{x}_t$ advected with the flow $\boldsymbol{u}_t(\boldsymbol{x}_t)$, $\dot{\boldsymbol{x}}_t = \boldsymbol{u}_t(\boldsymbol{x})$. Consider how an infinitesimal separation vector, $\delta\boldsymbol{x}_t$, at this tracers position deforms as it is advected by the flow,

$$\frac{d\delta\boldsymbol{x}_t}{dt} = \boldsymbol{u}_t(\boldsymbol{x}_t + \delta\boldsymbol{x}_t) - \boldsymbol{u}_t(\boldsymbol{x}_t), \tag{3.16}$$

$$= \mathbb{A}_t(\boldsymbol{x}_t)\delta\boldsymbol{x}_t, \tag{3.17}$$

Here, we have assumed that the velocity field is smooth at very small scales, so that the velocity gradient $\mathbb{A}_t$ is well defined. Order $\delta\boldsymbol{x}_t^2$ terms have been ignored in this equation. This equation has the formal solution,

$$\delta\boldsymbol{x}_t = \mathscr{T} e^{\int_0^t \mathbb{A}_s \mathrm{d}s}\delta\boldsymbol{x}_0, \tag{3.18}$$

where $\mathscr{T}$ denotes time ordering. The above equation describes how the separation vector deforms as it is advected along with a tracer. We can define a deformation tensor $\mathbb{F}_t = \mathscr{T} e^{\int_0^t A_s \mathrm{d}s}$, which describes this deformation. This tensor describes not just how separations evolve but also how fluid volumes deform in time. Assuming singlevaluedness of the flow $\boldsymbol{u}$, it follows that the deformation tensor must be invertible. When the matrix $\mathbb{F}_t$ is invertible, the polar decomposition theorem [36] ensures that $\mathbb{F}_t$ can be uniquely

decomposed into a rotational component, and a deformation component, $\mathbb{F}_t = \mathbb{R}_t\mathbb{U}_t = \mathbb{V}_t\mathbb{R}_t$. Here $\mathbb{R}_t$ is a rotation matrix, and $\mathbb{U}_t$ and $\mathbb{V}_t$ are called the right stretch tensor and left stretch tensor, respectively. The difference between the two decompositions arises because either the rotation or the stretch may be performed first in order to obtain the same deformation. Even though the result is the same, the different ordering of stretching and rotation means that the left and right stretch tensors have different eigenvectors. When the stretch is performed first, with $\mathbb{U}_t$, the stretching of the fluid parcel takes place along the direction of initial stretching, described by the eigenvectors of the strain-rate matrix at time zero, $\mathbb{S}_0$. Thus, the eigenvectors of $\mathbb{U}_t$ coincide with those of $\mathbb{S}_0$. This deformed parcel is then rotated by $\mathbb{R}_t$ to its final position. In contrast, when the rotation is performed first, the fluid parcel is first rotated by $\mathbb{R}_t$. This is followed by stretching by $\mathbb{V}_t$ along the *final* main stretching directions. Thus the information of the main directions of stretching after time t can be obtained in two ways, either by knowing the eigenvectors of $\mathbb{U}_t$ (same as the eigenvectors of $\mathbb{S}_0$) *and* the rotation matrix $\mathbb{R}_t$, or simply by knowing the eigenvectors of $\mathbb{V}_t$.

Using the deformation tensor $\mathbb{F}_t$, it is possible to form two symmetric tensors, $\mathbb{M}_t = \mathbb{F}_t\mathbb{F}_t^\intercal = \mathbb{V}_t^2$ and $\mathbb{C}_t = \mathbb{F}_t^\intercal\mathbb{F}_t = \mathbb{U}_t^2$ called the left Cauchy-Green tensor and right Cauchy-Green tensor, respectively. Then, the left Cauchy-Green tensor has the same eigenvectors as $\mathbb{V}_t$, which are the main stretching directions of the fluid parcel after time t. In particular, the eigenvector with the largest eigenvalue is termed the Lagrangian stretching direction. This Lagrangian stretching direction forms a reference direction particular to the flow which a tracer has experienced. It can be used as a reference even in homogeneous and isotropic flows which do not have a preferred direction by definition.

3.2 Turbulent channel flow

Turbulent flows with boundaries are ubiquitous in Nature. They have important differences compared to flows far from boundaries. In contrast to homogeneous and isotropic flows, the presence of the boundary breaks homogeneity by breaking translational invariance of the flow in the direction normal to the boundary. However, isotropy at the small scales has been postulated to be restored at infinite Reynolds numbers [37]. Flows at more

realistic Reynolds numbers however show small scale anisotropies [38, 39] and have been a subject of much interest. A turbulent channel flow is a prominent example of a wall-bounded flow relevant for industrial application. In addition, the behaviour near a channel boundary is a good playground for understanding wall-bounded turbulent flows which occur often in Nature, one example is river beds. The description of the turbulent channel flow here follows the discussion in Ref. [40].

A turbulent channel flow is usually taken to be a fluid flow in a straight channel with a rectangular cross-section [41]. The length and width of the channel are taken to be much larger than the height. The mean flow is along the length of the channel, and this direction is called the stream-wise direction. The direction along the height of the channel is called the wall-normal direction, and the one along the width is called the span-wise direction. The stream-wise, span-wise and wall-normal directions are denoted by $\hat{\mathbf{x}}, \hat{\mathbf{y}}$ and $\hat{\mathbf{z}}$ respectively in this thesis, see Fig. 3.1. The flow is typically driven by a pressure gradient along the length of the channel. No-slip boundary conditions are imposed for the velocity at the top and bottom boundary in the wall-normal direction. Periodic boundary conditions are imposed in the span-wise and stream-wise directions. The dimensional quantities for the system then are the height of the channel $2h$, the pressure gradient across the channel Δp, the fluid kinematic viscosity ν_f, and the fluid mass-density ρ_f. The pressure gradient in turn determines the wall shear stress τ_wall. The wall shear stress can be used to define the wall friction velocity as $u_\tau = \sqrt{\tau_\mathrm{wall}/\rho_\mathrm{f}}$.

As mentioned in Section 3.1, turbulent flows are typically characterised by the Reynolds number. In the case of a turbulent channel flow, the relevant Reynolds number is called the friction Reynolds number, Re_τ. This is defined in terms of the wall friction velocity u_τ and the channel half-height h as $\mathrm{Re}_\tau = hu_\tau/\nu_\mathrm{f}$.

The velocity in a turbulent channel flow exhibits both spatial and temporal fluctuations. However, the average velocity profile gives an idea of the typical flow velocities in different regions of the channel. Near the channel center, the velocity is large and the velocity profile is rather flat, as shown in Figure. 3.1. As the channel boundary is approached the mean velocity drops off, until it approaches zero at the boundary, due to the no-slip boundary condition imposed there. In all, the boundary layer consists of three pieces [40]: a layer very close to the wall called the viscous boundary layer, a far layer called the log-layer, and a crossover region called the buffer layer . The total thickness

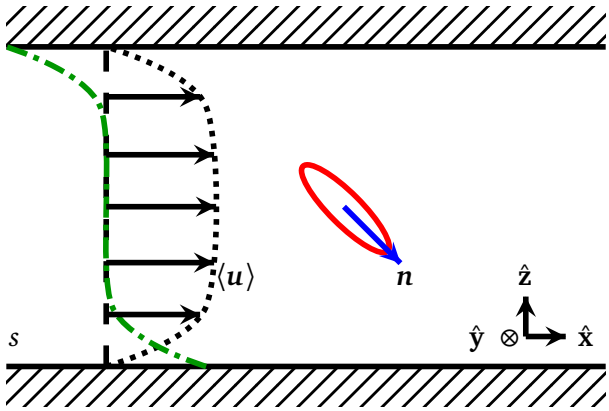

Figure 3.1: Illustration of an ellipsoidal particle with orientation vector $\boldsymbol{n}$ suspended in a channel flow. The stream-wise and wall-normal directions are denoted by $\hat{\mathbf{x}}$ and $\hat{\mathbf{z}}$ respectively. The span-wise direction $\hat{\mathbf{y}}$ points into the plane of the page. The black dotted line illustrates the mean stream-wise velocity $\langle u \rangle$, and the green dash-dotted line illustrates the mean shear rate s.

of the boundary layer decreases with increasing Reynolds number.

In a turbulent channel flow, near the channel center the flow resembles homogeneous isotropic turbulence. In ref. [42] the authors examined intermittency in a turbulent channel flow at Reynolds number $\mathrm{Re} \approx 3000$ and found that results near the channel center were consistent with homogeneous isotropic turbulence. The authors of Ref. [43] analysed the distributions of the second invariant $Q = -\frac{1}{2}\mathrm{Tr}\mathbb{A}^2$ in turbulent channel flows at friction Reynolds number $\mathrm{Re}_\tau = 180, 400, 800$, and 1270 and found good agreement between the channel center and homogeneous isotropic turbulence. Pumir [44] reported a small anisotropy near the channel center for turbulent channel flows at $\mathrm{Re}_\tau \approx 999$. However the anisotropy was larger for the third moment of the velocity gradient tensor than the second moment. In Chapter 7 the highest moment we will be interested in will be the second moment so we safely assume isotropy near the channel center. Note, however, in some cases certain third order moments have been shown to be important for the angular dynamics of particles in turbulent flows [45].

Near the channel boundary, the mean stream-wise velocity increases as a function of the distance from the channel boundary. This also implies that one of the mean shear-rates, $\langle A_{xz} \rangle = s$ near the channel boundary is

non-zero. In addition, due to the presence of no-slip boundary conditions, the fluctuations in span-wise and stream-wise gradients of velocities are dampened. In summary, the region near the channel boundary exhibits a large mean shear-rate s as well as very small fluctuations. See Ref. [46] for a detailed account of velocity-gradient statistics in turbulent channel flows.

3.3 Random velocity-fields

It turns out that not all properties of turbulent flow fields are important to describe the distributions of particles in turbulence. When the particles of interest are much smaller than the Kolmogorov length, and move slow enough relative to the fluid, the properties which affect the particle dynamics are: the small-scale fluid correlation length, the small-scale correlation time, and the Lagrangian statistics of the fluid-flow fluctuations. In order to study the dynamics of small,slowly moving particles, it siffices to use a random, Gaussian velocity-field to model turbulence [6, 7, 19, 20, 47, 48, 49, 50]. The physical parameters describing a single-scale, Gaussian random field are the Eulerian correlation time τ, the correlation length η, and C_0, the magnitude of fluctuations.

The velocity field for a Gaussian random flow in $d-$spatial dimensions is implemented as follows: first one generates a scalar random Gaussian field $\phi(\boldsymbol{x}, t)$ [51],

$$\phi(\boldsymbol{x}, t) = (2\pi)^{d/4} \left(\frac{\eta}{L}\right)^{d/2} \sqrt{C_0} \sum_{\boldsymbol{k}} a_{\boldsymbol{k}}(t) e^{i\boldsymbol{k}\cdot\boldsymbol{x} - \frac{k^2\eta^2}{4}}. \tag{3.19}$$

Here η sets the correlation length of the random flow, L is the system size, and C_0 quantifies the magnitude of fluctuations. The coefficients $a_{\boldsymbol{k}}$ are complex random numbers which must satisfy $a_{\boldsymbol{k}} = a^*_{-\boldsymbol{k}}$ so that ϕ remains real. The coefficient a_0 must be Gaussian distributed with mean zero and variance 1. The other coefficients must have their real and imaginary parts both distributed with mean zero and variance $\frac{1}{2}$, so that $\langle a_{\boldsymbol{k}} a^*_{\boldsymbol{k}} \rangle = 1$. The coefficients can be generated from independent Ornstein-Uhlenbeck processes,

$$\dot{a}_{\boldsymbol{k}}(t) = -\frac{1}{\tau} a_{\boldsymbol{k}}(t) + \sqrt{\frac{2}{\tau}} \xi(t), \tag{3.20}$$

so that τ sets the correlation time of the coefficients $a_{\boldsymbol{k}}$ and of the field ϕ. Here $\xi(t)$ is a complex-valued white-noise process. From this construction one obtains Gaussian random fields $\phi(\boldsymbol{x}, t)$ with correlation functions,

$$\langle \phi(\boldsymbol{x}, t)\phi(\boldsymbol{x}', t')\rangle = C_0 e^{-\frac{|x-x'|^2}{2\eta^2} - \frac{|t-t'|}{\tau}}. \tag{3.21}$$

Thus we have generated a scalar random field $\phi(\boldsymbol{x}, t)$ which has Gaussian spatial correlations and exponential time correlations. Velocities and velocity gradients may be obtained from ϕ by considering spatial derivatives. A more detailed discussion can be found in [51]. The two main advantages of using the Gaussian random field are reduced computational complexity, and that in the limit $\tau \to 0$ it is possible to use the diffusion approximation in order to obtain analytical results which can lead to important insights about physical mechanisms.

Despite their successes, Gaussian random velocity fields differ from turbulence in several aspects, here we state three. First, the distribution the velocity gradients at a fixed position are usually chosen to be Gaussian distributed [6] whereas turbulent flows at high enough Reynolds numbers show non-Gaussian fluctuations [35]. Second, the convective term, $\boldsymbol{u} \cdot \nabla \boldsymbol{u}$, in the Navier-Stokes equations leads to coupled modes. This in turn leads to an energy cascade where energy is transferred from large scales to small scales and dissipated at small scales by viscous friction [3]. At very small scales, the velocity varies smoothly as a function of space [37, 40]. This importance of various length scales leads to the multi-scale picture of turbulence [3, 40]. The statistical model we use has one length scale, and it is meant to model the small scale smooth fluctuations [6]. Finally, turbulence is self advecting due to the convective term, a phenomenon known as sweeping. The random velocity field misses any effects due to sweeping. Nevertheless, statistical models for particles in turbulence based on Gaussian, random velocity-fields reproduce not only the qualitative [6], but also quantitative aspects of the dynamics of particles in turbulence as shown in Refs. [52, 53] as well as paper B.

4 Four models for particles in flows

Having briefly discussed some fluid flows in Chapter 3, next we must ask how these flows affect particles immersed in them. The force applied on a particle by the surrounding fluid is a direct consequence of the stress applied on the particle surface by the fluid [14, 54]. This force, however, can only be calculated in closed form for slowly varying flows and simple particle shapes [11]. One simple example is Stokes force [11, 14],

$$\boldsymbol{F} = -6\pi\nu_{\mathrm{f}}\rho_{\mathrm{f}}a[\boldsymbol{u}(\boldsymbol{x}) - \boldsymbol{v}]. \tag{4.1}$$

which gives the force experienced by a spherical particle of radius a in creeping flow conditions. The force experienced by the particle, Eq. (4.1) depends upon the particle velocity $\boldsymbol{v}$ relative to the undisturbed flow-velocity at the particle position, $\boldsymbol{u}(\boldsymbol{x}, t)$.

The Stokes force, Eq. (4.1), is valid when $\mathrm{Re} = 0$ in the Navier-Stokes equation, Eq. (3.7). It successfully predicts the hydrodynamic force on small particles moving slowly compared to the flow. But it does not account for the inertia of the fluid [55], nor for the effects of unsteadiness which may be important when the flow around the particle changes with time [56].

In other words, the Stokes equations is an appropriate description of the force on the particle when the approximations made in deriving it are satisfied. However, which approximation to use depends not only on the system under study, but also on the question of interest. In this chapter I introduce four models which treat various aspects of the dynamics of particles in turbulence relevant for the questions considered in this thesis.

In Section 4.1, I introduce the correlated random-walk model which describes the dynamics of small but heavy particles. In Section 4.2 I describe a model for the angular dynamics of advected spheroids. In Section 4.3 I discuss two models describing the effect of hydrodynamic and electrical interactions on the dynamics of spheres settling under the effect of gravity.

4.1 Correlated random-walk model

The correlated random-walk model is a one-dimensional map with random but spatially -correlated increments [57]. Deutsch first used this model to describe a “path-coalescence” transition [58, 59]. The path-coalescence transition

describes a bifurcation where nearby particle trajectories coalescence together, instead of separating exponentially as a parameter is varied. Pikovsky [57] studied the distribution of separations near the transition point. Wilkinson & Mehlig [60] discussed the applications of the path-coalescence transition, while Wilkinson *et al.* [61] described how distributions of separations depend upon the parameters of the model. This model is used in paper A to study the distributions of inertial particles in random flows.

In this model, the particles are restricted to a domain $[0, L)$ with periodic boundary conditions. This introduces a length scale L in the system. We assume that a point particle located at position x_n at timestep n experiences a displacement given by $f_n(x_n)$,

$$x_{n+1} = x_n + f_n(x_n). \tag{4.2}$$

We further assume that the displacements $f_n(x_n)$ are Gaussian random functions with zero mean, which are correlated in space but uncorrelated in time,

$$\langle f_n(x_n) f_m(y_m)\rangle = \delta_{nm}\sigma^2 \exp\left(-\frac{(x_n - y_m)^2}{2\eta^2}\right). \tag{4.3}$$

Here, σ is the mean-squared displacement, and η is the correlation length. The average $\langle\cdot\rangle$ denotes an average over different realizations of the Gaussian random functions. The Gaussian random functions, $f_n(x_n)$, in Eq. (4.3) may be generated as described in the previous chapter. In summary, Eqs.(4.2)-(4.3) define the correlated random walk model. Fig. 4.1, shows some realisations of the correlated random walk model.

The model has two dimensionless parameters, $\alpha \equiv \frac{\sigma}{\eta}$ and $l \equiv \frac{L}{\eta}$. The parameter α is a measure of the magnitude of the particle position increments, and is analogous to the inertia parameter in statistical models. The parameter l quantifies the separation of length scales in the system. In order to minimise effects due to the system boundary, we will work in the regime $l \gg 1$.

Relative separation of correlated random walkers

Consider two correlated random walkers, with positions at time step n given by x_n and y_n. Linearising in the separation $\Delta x_n = x_n - y_n$, we obtain the

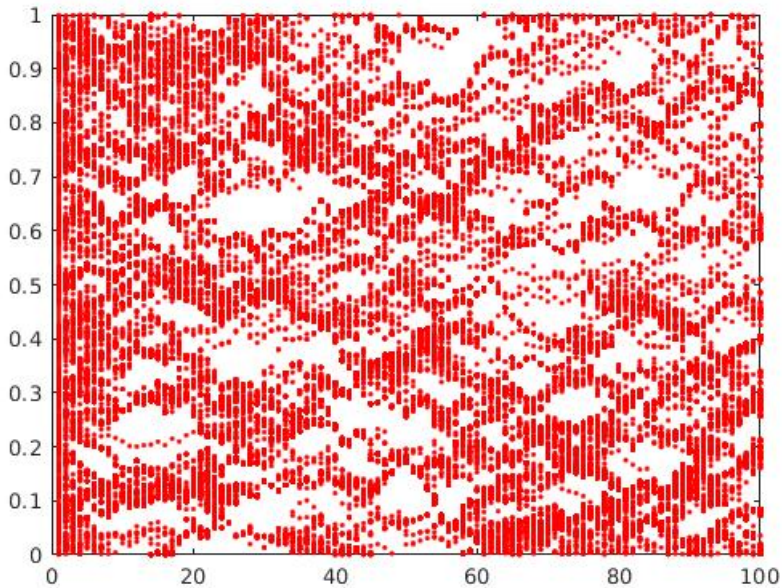

Figure 4.1: A snapshot of the correlated random walk model simulation depicting clustering. The Figure is borrowed from my Licentiate thesis [62].

following set of equations:

$$x_{n+1} = x_n + f(x_n), \tag{4.4}$$
$$\Delta x_{n+1} = \Delta x_n + f'(x_n)\Delta x_n, \tag{4.5}$$

where f' denotes the derivative of the function f. Using Eq. (4.3) one can show that $f_n(x_n)$ and $f_n'(x_n)$ are uncorrelated. Thus the equation for the separation Δx_n decouples from the equation for x_n. We denote $A_n \equiv f'(x_n)$, whose correlation function can be derived using Eq. (4.3). The single point statistics of A_n are easy to compute. We have simply that A_n is a Gaussian random variable with zero mean and variance $\langle A_n A_m \rangle = \delta_{nm}\alpha^2$. Thus we end up with

$$\Delta x_{n+1} = (1 + A_n)\Delta x_n. \tag{4.6}$$

It is clear from Eq. (4.6) that $A_n < -1$ for any n leads to Δx_{n+1} obtaining a sign opposite to that of Δx_n, meaning that the particles have crossed each other. These trajectory crossings are analogous to caustics in continuous-time models [6].

4.2 A model for angular dynamics of spheroids

The flow around small particles is well approximated by Stokes flow, also known as creeping flow [11]. In this approximation, the equations describing the motion of the center-of-mass $\boldsymbol{x}(t)$ of a small, advected spherical particle read [18],

$$\dot{\boldsymbol{x}}(t) = \boldsymbol{u}(t), \tag{4.7}$$

where $\boldsymbol{u}$ is the fluid velocity. The equations describing the orientation $\boldsymbol{n}(t)$ of a small, neutrally buoyant, inertia-less particle in a creeping flow were first derived by Jeffery [63]. These equations, known as Jeffery's equations, read,

$$\dot{\boldsymbol{n}}(t) = \mathbb{B}(t) \cdot \boldsymbol{n}(t) - \boldsymbol{n}(t)^{\intercal}\mathbb{B}(t)\boldsymbol{n}(t). \tag{4.8}$$

where $\mathbb{B} = \mathbb{O} + \Lambda\mathbb{S}$ and $\mathbb{O}$ and $\mathbb{S}$ are the anti-symmetric and symmetric part of the fluid velocity-gradient matrix, respectively. Λ is the particle shape parameter, defined as $\Lambda = \frac{\lambda^2-1}{\lambda^2+1}$ where λ is the aspect ratio of the spheroid.

The aspect ratio λ is defined as the ratio of the semi-axis from the center to the pole, a, and the semi-axis from the center to the equator b,

$$\lambda = \frac{a}{b}. \tag{4.9}$$

Eq. (4.8) is used in paper B to study alignment statistics of rods in a turbulent channel flow.

Here I sketch the derivation of Jeffery's equation. In Section 3.1 we have seen the dedimensionalised form of the Navier-Stokes equations, Eqs. (3.7)-(3.8). We left the characteristic length scale L_0 and velocity scale U_0 unspecified because they depend on the system of interest. In the context of particles in turbulent flows, a natural length scale is the size of the particle. Assuming a spherical particle the size can be measured by the radius of the sphere, a. Which gives the *particle* Reynolds number, $\mathrm{Re}_p = \frac{aU_0}{\nu_\mathrm{f}}$. Further since we are interested in small particles, assuming $a \ll \frac{\nu_\mathrm{f}}{U_0}$, we have that $\mathrm{Re}_p \ll 1$ and thus the Stokes flow, described by solutions to Eqs. (3.10), is justified for the particle-flow system.

The equation (4.8) arises from a solution of the Stokes equations with no-slip boundary conditions on a spheroidal particle's surface, with a linear flow at infinity. Due to no-slip boundary conditions, the flow induces a stress on the particle surface. Formally, integrating the stress over the particle's surface gives the force and torque on the particle. Knowing the mass and moment-of-inertia tensor of the particle, the translational and angular velocities are obtained from the force and torque using Newton's second law. Practically, solving Stokes equations around a particle is hard, and thus it is hard to obtain the fluid stress at the particle surface. One way to proceed is by realising that this is a boundary value problem for the Stokes equation. Thus, a solution can be found using the Green's function for Stokes equations and using the multipole expansion to obtain corrections to the point particle approximation [11]. The result for spheroidal particles is given by (4.8).

4.3 Two models for two interacting spheres

So far we have considered models valid either for a single particle, or for two particles whose separation is much larger than their radius. But what happens when two spherical particles approach close enough so that they interact

through the fluid and possibly collide? In order to model particle collisions, their interactions at small separations must be taken into account. In this Chapter I introduce two models which account for particle interactions.

The first model ignores fluid inertia, particle inertia (Stokes number, St), charges, and unsteady effects. But the upshot of this model is that it includes hydrodynamic interactions valid for all separations and non-continuum effects (quantified by the Knudsen number, $\mathrm{Kn} = l/\overline{a}$ where l is the mean-free-path of air and $\overline{a} = (a_1 + a_2)/2$ is the mean droplet radius of two droplets with radii a_1 and a_2) near contact. This model was first used by Refs. [64, 65] in order to study collisions of settling droplets in steady and turbulent flows. This model is used in paper D to study how bifurcations affect the collision dynamics of neutral droplets in a straining flow.

The second model includes fluid inertia (particle Reynolds number, Re_p) and particle inertia ($\mathrm{St} = \frac{v\tau_p}{a}$ where a is the droplet radius, v is the typical droplet velocity, and $\tau_p = \frac{2\rho_p}{9\rho_f}\frac{a^2}{\nu_f}$ is the particle relaxation time), unsteadiness (Strouhal number, $\mathrm{Sl} = \frac{a}{v\tau_c}$, and τ_c is the droplet acceleration timescale taken to be the acceleration due to electrical force), and charges (Coulomb number, $\mathrm{Cu} = \frac{2k_e q_1 q_2}{m^* V^2 (a_1+a_2)}$ where k_e is Coulomb's constant, q_1 and q_2 are the charges on the two droplets with radii a_1 and a_2, respectively, $m^* = \frac{m_1 m_2}{m_1+m_2}$ is the reduced mass of the two droplets with masses m_1 and m_2, and $V = |\boldsymbol{V}|$ is the magnitude of the relative velocity of the droplets), but not non-continuum effects. However, the downside of this generalisation is that the model is only valid when the droplet separation remains larger than a few droplet radii. This model is used in paper C to study the collision dynamics of charged droplets settling in still air.

4.3.1 Uniformly valid model including Kn effects

We start by ignoring the effects of fluid inertia and unsteadiness, and by assuming that the flow surrounding the particles is a linear function of position. In this creeping flow approximation, the fluid surrounding the spheres is described by the Stokes equation, Eq. (3.10). Because the Stokes equation is linear, the slip velocity $\boldsymbol{v}_i - \boldsymbol{u}_i$ of spheres $i = 1, 2$ in a linear flow is a linear function of the hydrodynamic forces, F_1^h and F_2^h, acting on the particles and

of the strain $\mathbb{S}$ that the particles experience [11],

$$\begin{pmatrix} \boldsymbol{v}_1 - \boldsymbol{u}_1 \\ \boldsymbol{v}_2 - \boldsymbol{u}_2 \end{pmatrix} = \begin{pmatrix} \mathbf{a}^{(11)} & \mathbf{a}^{(12)} & \mathbf{g}^{(1)} \\ \mathbf{a}^{(21)} & \mathbf{a}^{(22)} & \mathbf{g}^{(2)} \end{pmatrix} \begin{pmatrix} \mu^{-1}\boldsymbol{F}^h_1 \\ \mu^{-1}\boldsymbol{F}^h_2 \\ \mathbb{S} \end{pmatrix}. \tag{4.10}$$

The tensors $\mathbf{a}^{(\alpha\beta)}$ and $\mathbf{g}^{(\alpha)}$ are called mobility tensors and depend upon the particle separation, $\boldsymbol{R} = \boldsymbol{x}_2 - \boldsymbol{x}_1$, upon the radii of the two spheres, a_1 and a_2, and upon the boundary conditions imposed at the fluid-particle boundary [11]. The tensors $\mathbf{a}^{(\alpha\beta)}$ have rank 2 while the tensors $\mathbf{g}^{(\alpha)}$ have rank 3. The appropriate boundary conditions for small water droplets in air is the no-slip boundary condition, and in this thesis we only consider this boundary condition.

In the case of axisymmetric particles, such as spheres, the mobility tensors may be written in terms of scalar functions:

$$a^{(\alpha\beta)}_{ij} = x^{(\alpha\beta)}_a \frac{R_i R_j}{R^2} + y^{(\alpha\beta)}_a \left(\delta_{ij} - \frac{R_i R_j}{R^2} \right), \tag{4.11}$$

$$g^{(\alpha)}_{ijk} = x^{(\alpha)}_g \left(\frac{R_i R_j}{R^2} - \frac{1}{3}\delta_{ij} \right) \frac{R_k}{R} + y^{(\alpha\beta)}_g \left(\frac{R_i}{R}\delta_{jk} + \frac{R_j}{R}\delta_{ik} - 2\frac{R_i R_j R_k}{R^3} \right), \tag{4.12}$$

where $x^{(\alpha\beta)}_a$ and $y^{(\alpha\beta)}_a$ are the radial and tangential scalar functions, respectively, corresponding to the mobility tensor $\mathbf{a}^{(\alpha\beta)}$, and $x^{(\alpha\beta)}_g$ and $y^{(\alpha\beta)}_g$ are the radial and tangential scalar functions, respectively, corresponding to the mobility tensor $\mathbf{g}^{(\alpha)}$. Jeffrey & Onishi [26] and Jeffrey [66] described how to compute the scalar functions with no-slip boundary conditions using the twin-multipole method. Their results are summarised in Ref. [11]. Other authors have used different methods to compute the mobility functions, such as the reflection method [14] and bispherical coordinates [67, 68]. The resulting mobility functions are uniformly valid for all particle separations: from large separations all the way up to contact. Using Eq. (4.11) and a similar equation for $\mathbf{g}^{(\alpha\beta)}$, and assuming that the only external force acting on the droplets is due to gravity, $\boldsymbol{g} = -g\hat{\mathbf{e}}_3$, the relative velocity $\boldsymbol{V} = \boldsymbol{v}_2 - \boldsymbol{v}_1$

can be written as,

$$V_i = S_{ij}R_j - \left[A\frac{R_iR_k}{R^2} + B\left(\delta_{ik} - \frac{R_iR_k}{R^2}\right)\right]S_{kl}R_l \\ -\left[L\frac{R_iR_k}{R^2} + M\left(\delta_{ik} - \frac{R_iR_k}{R^2}\right)\right]\frac{2\rho_p}{9\rho_f}\frac{(a_2^2 - a_1^2)g}{\nu_\mathrm{f}}\,\delta_{k3}\,, \tag{4.13}$$

where now A and B are the radial and tangential mobility functions formed using the functions $x_g^{(\alpha)}$ and $y_g^{(\alpha)}$, respectively, while L and M are the radial and tangential mobility functions formed using the functions $x_a^{(\alpha\beta)}$ and $y_a^{(\alpha\beta)}$, respectively. In paper D, following Ref. [64] we implemented the radial mobility functions using the results of Wang *et al.* [68] and the tangential mobility functions using those of Jeffrey & Onishi [26].

Effect of continuum breakdown

In addition to the hydrodynamic effects affecting droplet motion, continuum breakdown might become important if the interfacial separation between the droplets becomes comparable to the mean free path of air. In fact, within the continuum approximation, two spheres can never collide because the mobility functions decay to 0 linearly in the interfacial separation $\xi \equiv R - 2$ [10]. Sundararajakumar & Koch [69] argued that a collision is, however, possible due to continuum breakdown. They calculated how continuum breakdown, quantified by the Knudsen number Kn, modifies the radial resistance functions (related to the radial mobility functions by an inversion). They showed that in the non-continuum approximation, the mobility functions decay to 0 as $(\log\log\frac{\mathrm{Kn}}{\xi})^{-1}$. This allows droplets to collide in finite time [64]. In order to obtain uniformly valid radial mobility functions, the non-continuum mobilities (Eqs. (4.2) – (4.6) in Ref. [64]) are matched to the mobility functions A and L derived in the creeping-flow limit,

4.3.2 Far-field model including St, Re_p, Sl, Cu

The equations of motion for two inertial droplets with masses m_1 and m_2 read,

$$\dot{\boldsymbol{x}}_1 = \boldsymbol{v}_1, \tag{4.14}$$

$$\dot{\boldsymbol{x}}_2 = \boldsymbol{v}_2, \tag{4.15}$$

$$\dot{\boldsymbol{v}}_1 = \frac{1}{m_1}\boldsymbol{F}_1(\boldsymbol{x}_1, \boldsymbol{x}_2, \boldsymbol{v}_1, \boldsymbol{v}_2), \tag{4.16}$$

$$\dot{\boldsymbol{v}}_2 = \frac{1}{m_2}\boldsymbol{F}_2(\boldsymbol{x}_1, \boldsymbol{x}_2, \boldsymbol{v}_1, \boldsymbol{v}_2). \tag{4.17}$$

Here, the forces $\boldsymbol{F}_i, i = 1, 2$ depend on the positions and velocities of both droplets. These forces can be written in terms of the contribution due to hydrodynamic interaction and fluid inertia, $\boldsymbol{F}^{\mathrm{HI}}$, the contribution due to the unsteadiness, $\boldsymbol{F}^{\mathrm{history}}$, and the contribution due to electrical charges, $\boldsymbol{F}^{\mathrm{e}}$,

$$\boldsymbol{F}_i = \boldsymbol{F}_i^{\mathrm{HI}} + \boldsymbol{F}_i^{\mathrm{history}} + \boldsymbol{F}_i^{\mathrm{e}}, \quad i = 1, 2. \tag{4.18}$$

In the following I describe how each contribution is computed.

Effect of fluid inertia including hydrodynamic interactions

In some physical situations, deviations from the creeping-flow approximation can have a significant qualitative affect on the relative dynamics of two droplets. One example is the dynamics of two droplets with precisely the same size, examined by Klett & Davis [70]. Due to time-reversibility of Stokes flow, the separation between two spheres with the same radius cannot change in time. This symmetry, however, is broken by fluid inertia, quantified by the Reynolds number.

While no theory exists quantifying the effect of fluid inertia for arbitrary Reynolds number, modelling the fluid around the droplets by the Oseen equation allows for approximate solutions when $\mathrm{Re} \ll 1$. The Oseen equation is an approximate linearisation of the Navier-Stokes equation [14]. Candelier & Mehlig [55] used the Oseen to equation compute the effect of fluid inertia to leading order in Re_p, and in $1/R$ using the reflection method. The result is the force on the droplets as a function of the particles radii, their separation and the Reynolds number.

Effect of unsteadiness

The unsteadiness of the fluid flow due to breakdown of the quasi-steady approximation around an accelerating sphere might affect the spheres relative dynamics. The effect of unsteadiness, quantified by the Strouhal number Sl, was computed to leading order in Sl and for widely separated spheres by Ardekani & Rangel [71].

In order to obtain an equation of motion correct to leading order in the inverse inter-particle distance, I computed the asymptotic expressions in the limit of large separation for the forces described by Ardekani & Rangel [71]. The results are presented in the Appendix of paper C.

Electrical interactions

Finally, in addition to hydrodynamic interactions, the spheres might carry electrostatic charges. When two spheres carrying charges q_1 and q_2 are far apart, the electrostatic force $\boldsymbol{F}^{(e)}$ between them is well approximated by Coulomb's law,

$$\boldsymbol{F}^{(e)} = k_e \frac{q_1 q_2}{R^2} \hat{\boldsymbol{R}}. \tag{4.19}$$

This equation assumes that the two droplets are so far apart that they may be treated as point particles. However, when the droplets approach each other, the point-particle approximation breaks down giving rise to multipole interactions which cause the force between them to deviate from Coulomb's law. Assuming two perfectly conducting spheres, so that the charges on them redistribute much faster than the distance between the spheres changes, Lekner [72] computed the force between the spheres valid for all separations. In this thesis, however, we restrict ourselves to Coulomb's law.

5 Observables

Physical observables are measurable quantities which help to characterise the dynamics of particles in fluid flows. In this Chapter, I will discuss three observables of interest for particles in fluids. First, the Lyapunov exponent which determine the long-time behaviour of small separations or relative angles of particles. Second, multifractal dimensions which help to quantify the distribution of particles on a fractal attractor. Third, I discuss collision rates for spherical droplets.

5.1 Lyapunov exponent

The Lyapunov exponent describes how the separation between two particles which are initially infinitesimally close to each other evolves in time [73]. In one dimension it is defined as [4],

$$\lambda = \lim_{t\to\infty} \lim_{R_0\to 0} \frac{1}{t} \ln \frac{R_t}{R_0}. \tag{5.1}$$

Here R_t denotes the separation between the particles at time t. Consider how to compute the Lyapunov exponent in a one-dimensional system defined by the equation of motion,

$$\dot{x}_t = f(x_t). \tag{5.2}$$

Two particles, whose positions at time t are $x_t^{(1)}$ and $x_t^{(2)}$, and which evolve according to the above equation satisfy,

$$\dot{x}_t^{(2)} - \dot{x}_t^{(1)} = f(x_t^{(2)}) - f(x_t^{(1)}). \tag{5.3}$$

Assuming that the function f is smooth, the equation of motion for the separation $R_t = x_t^{(2)} - x_t^{(1)} \ll 1$ can be written,

$$\dot{R}_t = f'(x_t^{(1)}) R_t\,, \tag{5.4}$$

where f' denotes the derivative of f, and terms of order R_t^2 are ignored. The Lyapunov exponent then reads,

$$\lambda = \lim_{t\to\infty} \frac{1}{t} \int_0^t \mathrm{d}s\, f'(x_s^{(1)}). \tag{5.5}$$

5.2 Multifractal dimensions

Particles in turbulent flows are distributed on self-similar sets, called fractals, which are different from usual familiar sets such as points, lines or surfaces [20, 21, 22]. Where a line or a surface is characterised by an integer dimension, which is 1 for a line and 2 for a surface, a fractal instead has a fractional dimension. In other words, fractals do not fill out the complete volume of the space they inhabit, yet, neither do they collapse on a point, or a line, or a surface [4].

Yet, where a single dimension suffices to characterise familiar sets such as lines or surfaces, complicated fractals known as multifractals, may require more than one, and sometimes even an infinity of dimensions to completely characterise them [23]. The reason is that while points on a line are uniformly distributed: any two segments have the same density of points, the points on a multifractal may be inhomogeneously distributed. In order to quantify the degree of inhomogeneity, a spectrum of dimensions called multifractal dimensions may be used [74, 75].

The multifractal dimensions are denoted by D_q where the parameter q can take any real value [23, 74]. The dimension D_0 is called the box counting dimension and it quantifies the dimension of the set spanned by the fractal. In the case of simple familiar sets mentioned above, $D_0 = 1$ for a line and $D_0 = 2$ for a surface. But in the case of a fractal, D_0 takes a non-integer value. For a simple fractal with a homogeneous density everywhere, called a monofractal, the general fractal dimension $D_q = D_0$. But for a multifractal this is not the case. When q is an integer, and at least for dynamics restricted to one dimension, D_q has a physical interpretation: it quantifies the probability of finding q particles close together [23], discussed in more detail below.

Let us first discuss how particle distributions are quantified using multifractal dimensions. In d spatial dimensions, and for uniformly distributed particles, the probability of finding two particles at a distance R is

$$P(R) \sim R^{d-1}. \tag{5.6}$$

This is true of tracer particles in incompressible flows. However, observations of inertial particles in both compressible and incompressible flows lead to a different picture. Snapshots of simulations, see Fig. 2 in Ref. [76], show clearly that particles bunch together. Similar clustering is observed also for the correlated random-walk model, see Fig. 4.1. Numerical [76] and analytical

[77] calculation of the distribution of relative separations for inertial particles leads to a result which looks qualitatively similar to Eq. (5.6) but quantitatively different,

$$P(R) \sim R^{D_2-1}. \tag{5.7}$$

Here D_2 is known as the correlation dimension. Inertia affects the distribution of relative separations, and in fact, D_2 depends smoothly on the inertia of the particles [6, 76].

The fractal dimensions, D_q for general q, can be defined by considering the statistics of the particle number distribution associated to the fractal attractor. Consider the number of particles m_R in a sphere of radius R. The fractal dimensions D_q can be defined by a Lagrangian average of powers of m_R,

$$\langle m_R^{q-1} \rangle \sim R^{(q-1)D_q} \quad \text{as} \quad R \to 0. \tag{5.8}$$

In the one dimensional correlated random walk model, the Lagrangian average of m_R may be alternatively defined as [23],

$$\langle m_R^{q-1} \rangle = P(Y_n^{(q)} \leq R) \quad \text{with} \quad Y_n^{(q)} = \max_{1 \leq i,j \leq q} \{|x_n^{(i)} - x_n^{(j)}|\}. \tag{5.9}$$

Then, using Eq. (5.8) it follows that,

$$P(Y_n^{(q)} \leq R) \sim R^{(q-1)D_q} \quad \text{as} \quad R \to 0. \tag{5.10}$$

This equation shows that in a one-dimensional system, the multifractal dimension D_q can be related to the statistics of the separation between the two furthermost particles out of a set of q particles.

5.3 Collision rate

The study of collision rate of rain-droplets in clouds has a long history [10]. The collision rate is important in understanding the rapid formation of rain in turbulent clouds [7, 13, 17, 47, 78]. Droplets may collide due to gravitational settling [79] or because they are pushed towards each other due to turbulent strains [17]. The particles inertia may allow them to collide at large relative velocities [7, 47], increasing the collision rate. In this Section, I define the collision rate between two droplets of different radii, a_1 and a_2. I then discuss

how this collision rate depends on the strain-rate and on the relative settling velocities of two non-interacting droplets.

Consider a test droplet with radius a_1, surrounded by n_0 droplets per unit volume with radius a_2. The influx of droplets entering a sphere of radius R around the test sphere between times 0 and T, $j(R,T)$, is given by,

$$j(R,T) = -n_0 \int_0^T dt \int d\Omega\, P(R,\Omega,t) V_R(R,\Omega,t)\, \Theta[-V_R(R,\Omega,t)]. \quad (5.11)$$

Here $P(R,\Omega,t)$ is the pair-probability at time t of finding two droplets at separation R, and at solid angle Ω defined from the center of the test droplet. $V_R(R,\Omega,t)$ is the radial velocity at separation R and solid angle Ω at time t. Finally, the Heaviside step-function $\Theta[-V_R(R,\Omega,t)]$ ensures that only trajectories entering the sphere of radius R are counted.

The steady-state collision rate can be defined using the droplet influx as,

$$\mathscr{R} = \lim_{R\to a_1+a_2} \lim_{T\to\infty} \frac{j(R,T)}{T}. \quad (5.12)$$

The first limit $T \to \infty$ ensures that the collision rate does not depend on any transients. Note that it is assumed that the particle number density n_0 does not change as this limit is approached. Physically, this corresponds to assuming that T is much larger than all timescales associated to the particle relative-dynamics. But much smaller than the timescale at which the particle number density n_0 changes. The second limit $R \to a_1 + a_2$ ensures that the collision rate is well defined even if the relative velocity vanishes upon contact, or the pair-probability diverges upon contact.

Consider a simple model of non-interacting spheres with radii a_1 and a_2 settling in a simple straining flow defined by the flow field, $\boldsymbol{u}(\boldsymbol{x}) = \frac{s}{2}\hat{\mathbf{e}}_1 + \frac{s}{2}\hat{\mathbf{e}}_2 - s\hat{\mathbf{e}}_3$. The collision rate in this model depends upon the ratio of the settling velocity $v_g = \frac{2}{9}\frac{\rho_p}{\rho_f}(a_2^2 - a_1^2)g/\nu$ and the characteristic velocity due to strain, $v_s = \overline{a}s$. The collision rate can be computed exactly as a function of $Q = \frac{v_g}{v_s}$ [64],

$$\frac{\mathscr{R}}{n_0 s(a_1+a_2)^3} = \frac{\pi}{108}[c_+(Q) + H(2-Q)\, c_-(Q)]\,, \quad (5.13a)$$

$$c_\pm(Q) = (12+Q^2)^{\frac{3}{2}} \pm Q(36-Q^2). \quad (5.13b)$$

Here, H is the Heaviside step function.

When the dynamics is dominated by strain, $Q \ll 1$, Eq. (5.13a) reproduces how the collision rate scales with the strain-rate first computed by Saffman & Turner [17], $\mathscr{R} \sim n_0 s (a_1 + a_2)^3$. In the other limit, $Q \gg 1$, when the gravitational settling dominates over strain, the collision rate reproduces the result of Von Smoluchowski [79], $\mathscr{R} \sim n_0 (a_1 + a_2)^2 v_g$.

Part III
My work

6 Correlated random-walk model

Distributions of heavy particles in turbulent flows exhibit strong inhomogeneities, even when the underlying fluid flows are incompressible [19, 76, 80, 81]. Such inhomogeneities are important because they affect how often heavy particles in turbulent flows collide [16]. But which mechanisms give rise to these inhomogeneities? And how can one precisely quantify them? Much progress has been made on these questions, summarised in the review by Gustavsson & Mehlig [6]. Bec *et al.* [76] studied the distributions of heavy particles in DNS of turbulence. Statistical models of particles in random flows [19, 81] show similar clustering. The control over timescales in the statistical model allows to understand mechanisms such as caustic formation which contribute to small-scale clustering.

While Bec *et al.* [82] quantified the detailed distributions of advected particles in compressible flows by computing the multifractal dimensions of the attractors on which the particles cluster, only the correlation dimension D_2 was well understood for inertial particles [6]. Wilkinson *et al.* [77] used perturbation theory to compute the correlation dimension in the white-noise limit. Meibohm *et al.* [83] showed that in a one-dimensional continuous time model, the exponent D_2 depends non-analytically on the inertia parameter to leading order, and argued that this leads to failure of perturbation theory in a small inertia parameter [77]. While it was expected that this is a general phenomenon, the precise non-analytic dependence of the correlation dimension on the inertia parameter for other models was not known. The question then was, whether the correlation dimension in the simpler correlated random walk model shows similar non-analytic behaviour and if it could be computed to higher accuracy?

In summary, this work was based on two fundamental questions. First, what is the precise functional dependence of the correlation dimension D_2 on the inertia parameter for the correlated random walk model. Second, how can one completely classify the fractal attractor as a function of particle inertia. More precisely, how do the higher fractal dimensions, D_q for integer $q \geq 2$, depend upon the inertia parameter.

6.1 Results

In paper A we found a relation between the different fractal dimensions D_q,

$$D_q = \frac{D_2}{q-1}, \tag{6.1}$$

for integer $q \geq 2$. These fractal dimensions D_q characterise the multifractal attractor on which particles cluster in the correlated random-walk model. We found this expression by analysing how particle trajectories cross when the particles are close together. Consider q particles with positions at time-step n labelled by $x_n^{(i)}, i = 1, 2, \ldots, q$. The positions are updated using a realisation of the random function, f_n, at time step n. Now assume that the particles are close to each other so that it is possible to linearise the dynamics around the position of the first particle. The updates then read,

$$\begin{aligned}
x_{n+1}^{(1)} &= x_n^{(1)} + f_n[x_n^{(1)}], \\
x_{n+1}^{(2)} &= x_n^{(2)} + f_n[x_n^{(1)}] + f_n'[x_n^{(1)}](x_n^{(2)} - x_n^{(1)}), \\
&\vdots \\
x_{n+1}^{(q)} &= x_n^{(q)} + f_n[x_n^{(1)}] + f_n'[x_n^{(1)}](x_n^{(q)} - x_n^{(1)}).
\end{aligned}$$

In this approximation, we find that $x_{n+1}^{(i)} - x_{n+1}^{(1)} = (1 + f_n'[x_n^{(1)}])\,(x_n^{(i)} - x_n^{(1)})$, for $i = 2, \ldots, q$. This equation shows that in this linearised regime, the separations between any particle and the first particle is scaled by the same factor $(1 + f_n'[x_n^{(1)}])$. This, in turn, means that the spatial ordering of the particles remains the same if $f_n'[x_n^{(1)}] > -1$, and reverses if $f_n'[x_n^{(1)}] < -1$. We called these crossings linear crossings, because they are the only allowed crossings in the linear regime. We term any crossing where the ordering neither remains the same, nor simply reverses a non-linear crossing.

This observation has important consequences for the exponent D_q. In particular, using Eqs. (5.9) – (5.10) to compute D_q, it suffices to consider only the two furthest particles out of a set of q particles. In other words, $P(Y_n^{(q)} \leq R)$ should scale the same way as $P(Y_n^{(2)} \leq R)$ in the limit $R \to 0$ which gives $(q-1)D_q = D_2$.

Eq. (6.1) is strictly valid only in the limit $R \to 0$ through Eq. (5.10). This means that numerical verifications of this equation were sensitive to whether

the particles spent long times close together or whether they separated quickly, quantified by the Lyapunov exponent. In the regime where the Lyapunov exponent was negative, Eq. (6.1) was clearly visible in numerics. By contrast, when the Lyapunov exponent was positive, it became harder to observe this relation numerically. The reason is that in this regime, it was likely that non-linear trajectory crossings occured, leading to deviations from Eq. (6.1).

In this model, the correlation dimension D_2 exhibits a non-analytic dependence on the inertia parameter α given by,

$$\begin{aligned} D_2 \sim -1 + \frac{e^{-1/(2\alpha^2)}}{\sqrt{2\pi}}(4\alpha - 14\alpha^3 + 63\alpha^5 - \frac{905}{2}\alpha^7 + \dots) \\ + \frac{e^{-1/\alpha^2}}{2\pi}[16\gamma\alpha^2 - 4(3+28\gamma)\alpha^4 + (\frac{170}{3} + 700\gamma)\alpha^6 - \dots] \\ + \frac{e^{-1/\alpha^2}}{2\pi}\log(\alpha^2/2)[-8\alpha^2 + 56\alpha^4 - 350\alpha^6 + \dots]. \end{aligned} \tag{6.2}$$

This equation gives D_2 to next-to-leading non-perturbative order in α. In this model, for $\alpha \ll 1$, no analytic terms in α contribute to D_2 meaning that perturbation theory in α predicts $D_2 \sim -1$. This is in contrast to Ref. [77] where perturbation theory works very well for small inertia parameters. But it does not explain, not even qualitatively, the minimum in D_2 as a function of the inertia parameter. It is expected [83] that this minimum results from non-analytic contributions, which are missed in a perturbative expansion.

Note that both Refs. [82] and [84] reported that $(q-1)D_q$ becomes independent of q for q larger than a critical value in their models. Ref. [82] considered multifractal statistics for advected particles in compressible flows. Ref. [84] computed the spectrum of multifractal dimensions in a one-dimensional, continuous-time model of inertial particles in turbulence. Ref. [82] found that the reason $(q-1)D_q$ becomes independent of q is because of rare events when large number of particles become localised in infinitesimally small volumes. This is consistent with our model, where the analogous phenomenon is trajectory crossings.

7 Angular dynamics in a turbulent channel flow

This chapter briefly introduces paper B and the results described there. This study of angular dynamics in a turbulent flow was a collaboration with our colleagues Zhiwen Cui and Lihao Zhao in Beijing, China. They are experts in direct numerical simulations (DNS) of turbulence and the simulations of particles in turbulent channel flows discussed here are performed by Zhiwen Cui. We at the University of Gothenburg developed the theory and I performed the analytical calculations.

The goal of this project was to describe the alignment behaviour of slender rods in turbulent flows. While a turbulent channel flow is anisotropic, so the channel geometry defines a fixed reference frame [85], homogeneous isotropic turbulence (HIT) no such reference frame exits. Previous works studied alignment of small, slender rods in HIT with quantities local to the flow such as the eigenvectors of the strain-rate matrix and the vorticity vector [38], and the Lagrangian stretching direction [86]. We find that the Lagrangian stretching direction, defined as the leading eigenvector $\boldsymbol{e}_{L1}$ of the left Cauchy-Green tensor is the ideal candidate for studying alignment of slender rod-like axisymmetric particles for two reasons. First, it is statistically stationary in the long time, and second, infinitely slender rods align perfectly with $\boldsymbol{e}_{L1}$ in the long time limit.

A second motivation is that the relative angles of nearby particles in homogeneous isotropic turbulence show rare large fluctuations, quantified by the angular structure functions [30]. These angular structure functions, $S_p(r)$, are defined as [30],

$$S_p(r) = \langle |\psi(\boldsymbol{x}+\boldsymbol{r}) - \psi(\boldsymbol{x})|^p \rangle_r. \tag{7.1}$$

Here $\psi(\boldsymbol{x})$ denotes an angle describing the orientation of a particle at position $\boldsymbol{x}$, and the angle brackets denote an average over particle-pairs with inter-particle distance r. However, direct numerical simulations (see paper B) showed that for particles in a turbulent channel flow, the relative angles between nearby particles are larger for particles near a channel boundary than particles near the channel center. The question then is, which mechanisms lead to larger relative angles between nearby rods near the channel wall. One hope was that understanding relative alignment with a local direction might also shed some light on relative alignment of close-by particles.

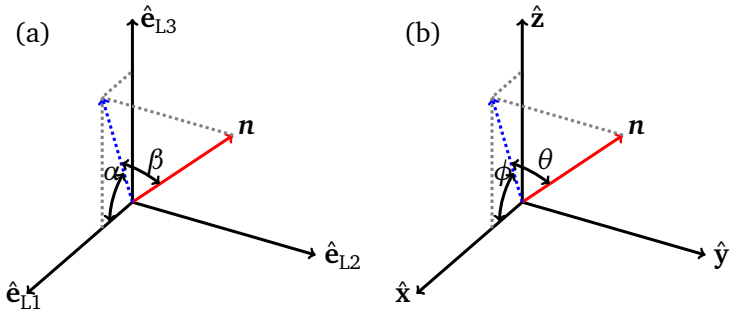

Figure 7.1: Euler angles used in analyzing the alignment of the particle-symmetry vector $\boldsymbol{n}$. (a) Coordinate system defined by the eigenvectors $\hat{\mathbf{e}}_{L1}(t), \hat{\mathbf{e}}_{L2}(t), \hat{\mathbf{e}}_{L3}(t)$ of the left Cauchy-Green tensor $\mathbb{M}(t)$. Here $\hat{\mathbf{e}}_{L1}$ and $\hat{\mathbf{e}}_{L3}$ are the expanding and contracting directions, while $\hat{\mathbf{e}}_{L2}$ is chosen to keep the coordinate system right-handed, and α, β are Euler angles in this reference frame. (b) Fixed Cartesian channel-coordinate system with basis vectors $\hat{\mathbf{x}}, \hat{\mathbf{y}}$, and $\hat{\mathbf{z}}$. Here $\hat{\mathbf{x}}$ is the stream-wise direction, $\hat{\mathbf{y}}$ the span-wise, and $\hat{\mathbf{z}}$ the wall-normal direction of the channel flow. The Euler angles are ϕ and θ.

A third aspect is the importance of slender fibre dynamics in industrial applications. The discussion in this paragraph follows Ref. [2]. A paper making machine uses paper pulp consisting of slender wood fibres suspended in a liquid. This pulp is pushed through a headbox into a thin layer which is further pressed and dried in order to make paper. The headbox serves two functions: (1) a compressing flow causes the slender fibres to align with the headbox wall, and thus with each other, and (2) turbulent fluctuations that lead to a more uniform distribution of fibres. Both are important for good quality paper. Thus for industrial applications it is interesting to study alignment of axisymmetric particles.

This work uses Jeffery's equations to model angular dynamics, both for simulations and theory. An important aspect is the use of a two dimensional toy model to understand the dynamics near the center of the channel. Near the channel boundary, approximating the mean shear-rate to be much larger than the magnitude of fluctuations of velocity-gradient matrix allow us to use a simplified equation of motion to describe the angular dynamics.

The notation used here is shown in Fig. 7.1. Here, $\hat{\mathbf{x}}, \hat{\mathbf{y}}, \hat{\mathbf{z}}$ denote the stream-wise, span-wise, and wall-normal directions of the turbulent channel flow.

We use two of the three Euler angles ϕ and θ in the flow-shear plane and out of this plane, respectively. The third Euler angle describes how the particle rotates around its axis of symmetry. This aspect is not considered. The vectors $\hat{\mathbf{e}}_{\mathrm{L1}}, \hat{\mathbf{e}}_{\mathrm{L3}}, \hat{\mathbf{e}}_{\mathrm{L2}}$ denote the Lagrangian stretching direction, the Lagrangian contracting direction and the middle eigenvector of the left Cauchy-Green matrix $\mathbb{M}_t$. In this coordinate frame, two of the three Euler angles are denoted by α and β.

The following sections present some results obtained in this study.

7.1 Alignment with the Lagrangian stretching direction

In this section we argue that the dynamics of an infinitely thin rod precisely follows the Lagrangian stretching direction in the long time limit. In Section 3.1 we discussed the left Cauchy-Green tensor. The Lagrangian stretching direction $\boldsymbol{e}_{L1}$ is the leading eigenvector of the left Cauchy-Green tensor. The steady state dynamics of the Lagrangian stretching direction follows the equation of motion [87],

$$\frac{d\boldsymbol{e}_{L1}}{dt} = \mathbb{A}\boldsymbol{e}_{L1} - (\boldsymbol{e}_{L1}^{\intercal}\mathbb{A}\boldsymbol{e}_{L1}). \tag{7.2}$$

Here $\mathbb{A}$ denotes the velocity-gradient matrix. First, this is the same as Jeffery's equation, Eq. (4.8), for $\Lambda = 1$. Second, the relative angle between $\boldsymbol{e}_{L1}$ and an infinitely slender rod always decreases, explained next. In two dimensions, assuming white-noise fluctuations for the velocity gradients, the Lyapunov exponent between an infinitely slender rod and the Lagrangian stretching direction can be calculated, Eq. (7.6), and is given by $\lambda^{(\alpha)} = -4$. In addition, there is no mechanism for ejecting the relative angle away from zero. This shows that in two dimensions with white-noise velocity gradient fluctuations the relative angle between $\boldsymbol{e}_{L1}$ and an infinitely slender rod exponentially decreases. DNS of turbulent channel flow show that the relative angle decreases exponentially there as well and that in the long time limit $\boldsymbol{e}_{L1}$ and an infinitely slender rod align perfectly. Thus, in the steady state, the orientation of an infinitely slender rod coincides with the Lagrangian stretching direction.

7.2 Tumbling time for slender rods near channel boundary

A slender rod advected near a turbulent channel boundary experiences a strong shear component as well as small fluctuations. We discussed in Paper B that the angular dynamics of this rod displays two qualitatively different regimes: the deterministic regime corresponding to strong shear and the stochastic regime corresponding to the effect of fluctuations close to alignment with the stream-wise direction. The equation for the angle ϕ, the Euler angle in the flow shear plane, reads (Eq. 4.5 in paper B),

$$\dot{\phi} = -\frac{s}{2}(1 - \Lambda \cos 2\phi) + \eta_\phi. \tag{7.3}$$

Here $\eta_\phi = A_{zx}$ is white noise with mean zero and variance $2D$. Fig. 7.2 shows some realizations of this process. The tumbling time for the rod, the time required for ϕ to go from $\phi = \pi/2$ to $\phi = -\pi/2$ is a random variable. In order to understand the statistics of the first time the process exits the interval $(-\pi/2, \pi/2]$, we compute the mean first exit time. For a theoretical background on calculation of mean exit times, see Ref [32], also discussed in Appendix of this work, and Appendix of Paper B.

In the Appendix of Paper B we presented an integral expression for the mean exit time along with the lowest order asymptotics. In fact, using a perturbation expansion it is possible to obtain the small and large $\delta\Lambda$ asymptotics to all orders, the result is presented in the Appendix.

The exit-time computed theoretically using a white-noise model matches extremely well with that computed in DNS of turbulence, see Fig. 6(**a**) in paper B. The reason is that near the channel boundary, the timescale of angular dynamics of slender rods is much slower than timescale of velocity-gradient fluctuations. This is precisely the white-noise approximation used in the calculation.

7.3 Large excursions of relative angles and relative separations

In this Section I discuss how the relative angular dynamics of two slender rods relates to their relative separation dynamics.

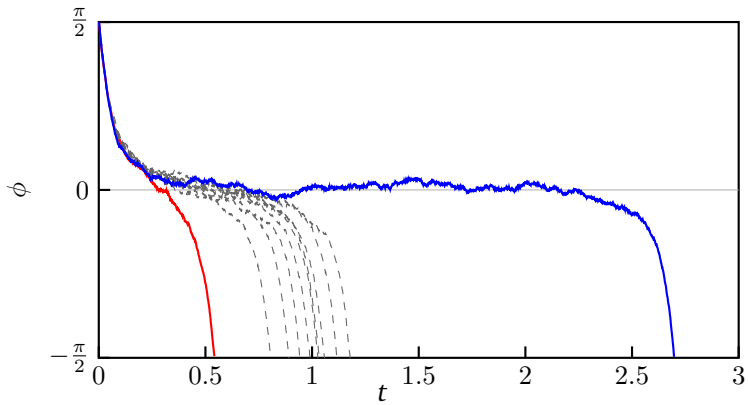

Figure 7.2: The process ϕ defined by Eq. (7.3) for values of the parameters $D = 0.01, s = 20, \Lambda = 0.95$. The dashed gray trajectories show typical behaviour. The red and blue trajectories show two extremes with exit times smaller and larger than the mean. The Figure is borrowed from my Licentiate thesis [62].

In the two dimensional toy model used for the center of the channel flow, the equations of motion of the interparticle distance r (where $\boldsymbol{r} = r[\cos\beta, \sin\beta]^{\intercal}$) between two small inertia-less, neutrally buoyant particles reads,

$$\dot{r} = r(\cos 2\beta S_{xx} + \sin 2\beta S_{xy}). \tag{7.4}$$

From the above equation, it is possible to compute the finite time Lyapunov exponent $\lambda_t^{(r)} \equiv \int_0^t \mathrm{d}s \frac{\dot{r}}{r}$,

$$\lambda_t^{(r)} = \int_0^t \mathrm{d}s\ (\cos 2\beta S_{xx} + \sin 2\beta S_{xy}). \tag{7.5}$$

Similarly, the finite time Lyapunov exponent for the relative angle α between two infinitely slender rods in two dimensions with angular orientations ϕ and $\phi + \alpha$ reads,

$$\lambda_t^{(\alpha)} = -2 \int_0^t \mathrm{d}s\ (\cos 2\phi S_{xx} + \sin 2\phi S_{xy}). \tag{7.6}$$

The dynamics of the angle β in Eq. (7.5) and the angle ϕ in Eq. (7.6) are described by Jeffery's equation with $\Lambda = 1$. Thus we see that in the long-time

limit, $\lambda_t^{(\alpha)} = -2\lambda_t^{(r)}$. Similar conclusions hold for the dynamics near the channel boundary. The Lyapunov exponent for the angular separations near a channel boundary can be calculated to obtain

$$\lambda^{(\delta\phi)} \sim -2\Lambda(s^2 D)^{1/3}. \tag{7.7}$$

Except for the factor of -2Λ, this is the same as the Lyapunov exponent for polymer elongation (and thus for particle separations) calculated in [88]. Thus, it seems that same quantities are responsible for large relative angles and large spatial separations. The mean spatial Lyapunov exponent for tracer particles is positive. Large negative fluctuations of the spatial finite time Lyapunov exponents cause tracers to approach each other. The situation for angular dynamics is reversed.

This relation between the spatial and angular Lyapunov exponents is a consequence of the way in which the fluid velocity-gradient matrix appears in both the equations of spatial and angular separations.

7.4 Distribution of relative angles between slender rods and the Lagrangian stretching direction

The DNS of slender rods in turbulence in paper B showed that distributions of relative angular separations between slender rods and the Lagrangian stretching direction showed plateaus at small relative angles and power law tails at large relative angles, both near the channel center and channel boundary.

Near the channel center we used a two dimensional toy model to qualitatively explain this behaviour in terms of large excursions caused by multiplicative amplification. Near the channel wall, however, the velocity-gradients fluctuate much faster than the slender rod rotates. Thus, we used a white noise model to predict exponents for the tails of the relative angle distributions,

$$P(\delta\phi, |\phi| \ll \phi_0) \sim \delta\phi^{-1-\frac{1}{\Lambda}}, \tag{7.8}$$

$$P(\delta\phi, |\phi| \gg \phi_0) \sim \delta\phi^{-1.5/\Lambda}. \tag{7.9}$$

Here ϕ is the Euler angle in the flow-shear plane of the Lagrangian stretching direction, $\delta\phi$ is the relative angle in the flow-shear plane between a slender rod and the Lagrangian stretching direction, and ϕ_0 is the mean value of ϕ. Computations of joint distributions of $\phi, \delta\phi$ in DNS by Zhiwen Cui [89] suggest that the the exponent in the two regimes for slender rods $\Lambda \approx 1$ are very nearly -2 and -1.5, respectively, showing excellent agreement with theory.

Mathematically, the power-law tails in the distribution of relative separations is a result of the scale invariance of the equations for motions for relative angles much larger than $\delta\Lambda$.

8 Collisions of charged droplets

In this chapter, I present the context for paper C, review the main results presented there, and discuss their implications. The goal of this study was to understand the dynamics of charged water droplets settling in quiescent air. The most important difference to papers A and B is that this study takes droplet interactions, both electrical and hydrodynamic, into account. The model used in this Chapter is described in Section 4.3.2. The problem is complicated by the myriad of competing effects that affect the droplet dynamics. Qualitatively, hydrodynamic interactions tend to bend the trajectory of one droplet around the other. On the other hand electrical forces are attractive for oppositely charged droplets and cause the droplets to approach each other. Both particle and fluid inertia allow droplets to detach from streamlines, and thus approach closer than in the absence of inertia. On the other hand, unsteady effects can cause a stronger hydrodynamic repulsion between droplets, compared to creeping flow. Finally, when the distance between the droplets surfaces is comparable to the mean free path of air, non-continuum effects become important. In summary, how should one account for these various effects?

8.1 Background and history of the problem

Historically, collisions of hydrodynamically interacting droplets have been analysed using the collision efficiency [10]. Consider how the collision efficiency is defined using grazing trajectories in the simple case of droplets settling under gravity. One starts from the equations of motion for the positions $\boldsymbol{x}_i$ and velocities $\boldsymbol{v}_i$ of the droplets $i = 1, 2$,

$$\dot{\boldsymbol{x}}_i = \boldsymbol{v}_i, \tag{8.1}$$

$$\dot{\boldsymbol{v}}_i = \frac{1}{m_i}\boldsymbol{F}_i(\boldsymbol{x}_1, \boldsymbol{x}_2, \boldsymbol{v}_1, \boldsymbol{v}_2). \tag{8.2}$$

Due to hydrodynamic interactions, the forces $\boldsymbol{F}_i$ are complicated functions of the positions and velocities [11, 14]. Therefore, the above equations are numerically integrated to find the grazing trajectory which delineates collisions from no-collisions. The impact parameter of the grazing trajectory

b_c is used to compute the collision efficiency, E,

$$E = \frac{b_c^2}{(a_1 + a_2)^2}, \tag{8.3}$$

where a_1 and a_2 are the radii of the two droplets. For comparison, in the absence of interactions, the critical impact parameter leading to collisions equals the sum of radii of two spheres, $b_c = a_1 + a_2$. This gives a collision efficiency $E = 1$. Because hydrodynamic interactions cause one droplets trajectory to bend around another, they reduce the impact parameter from its value in the non-interacting case.

While the picture presented above is insufficient when the droplets experience a steady or turbulent background flow, a similar comparison can be made in terms of the collision rate with hydrodynamic interactions, $\mathscr{R}_{HI}$, and without it, $\mathscr{R}_0$ [90],

$$E = \frac{\mathscr{R}_{HI}}{\mathscr{R}_0}. \tag{8.4}$$

This general definition allows to extend the idea of the collision efficiency beyond the simple case of settling droplets. Yet, the key component is still the grazing trajectory which differentiates collisions from no-collisions, at least for steady background flows.

In summary, the collision efficiency allows to understand the effect of any kind of interactions, regardless of whether they arise due to charges, hydrodynamics or non-continuum effects, using a single numerical quantity: the collision efficiency. However, the trajectory analysis employed to compute the collision efficiency might miss important physical effects which allow or prohibit collisions. While it allows a numerical quantification of the collision efficiency, it fails to illuminate the physical mechanisms which give rise to the observed collision efficiencies.

We took an alternative approach to analysing droplet collisions in paper C. In order to understand the mechanisms which lead to collisions of charged droplets settling in turbulence, we analysed the dynamics using dynamical systems theory. The field of dynamical systems was born more than 100 years ago as a tool to explain the motion of celestial bodies [91, 92]. Since then, it has been applied with great success to explain the behaviour of various physical systems [4, 73], chemical reactions [93], and biological processes [94].

8.2 Results

Using dynamical systems theory, we showed that the collision dynamics of charged droplets were qualitatively different from neutral ones, in a way that is mathematically well defined. Let us recap the mechanisms leading to neutral droplet collisions: neutral droplets settling under gravity collide because the breakdown of the continuum approximation at small interfacial separations [69] allows them to touch [64]. In other words, the collisions of neutral droplets are sensitive to strength of non-continuum effects, quantified by the Knudsen number, defined in Section 4.3. The smaller the Knudsen number, the stronger the hydrodynamic lubrication at small separations and the smaller the collision efficiency.

By contrast, we found that collisions of charged droplets are determined by stable manifolds of a saddle point. The saddle point in the dynamics results due to a balance between differential settling and Coulomb attraction. Differential settling tends to pull two differently-sized droplets apart, at long times. Coulomb attraction, however, competes with differential settling and tends to hold the droplets together giving rise to a fixed point in the relative dynamics. This fixed point is a saddle, whose location depends upon the relative strength of differential settling versus Coulomb attraction. The stable manifold of this saddle point delineates collision from no-collisions.

An important effect of the dynamics described in the previous paragraph is that it makes the collision outcomes independent of non-continuum effects as long as the stable manifold of the saddle point is far from the collision sphere. The reason is precisely that now the collision outcome is determined not by a grazing trajectory but by a stable manifold. A grazing trajectory, by definition, is tangential to the collision sphere upon contact and thus is sensitive to dynamics infinitesimally close to the collision sphere. A stable manifold, however, may occur arbitrarily far from the collision sphere, well outside the continuum breakdown regime. In that case, the stable manifold *does not* graze the collision sphere.

9 Bifurcations in droplet collisions

In this chapter, I present the context for paper D, review the main results presented there, and discuss their implications. In paper D , we explain the collision rate of neutral droplets settling in a straining flow, first studied by Dhanasekaran *et al.* [64]. The model used here is described in Section 4.3.1. Hydrodynamic interactions to all orders are taken into account, in contrast to paper C where only leading order effects were considered. Continuum breakdown at separations comparable to the mean free path of air is considered as well [69]. On the other hand, electrical interactions, fluid inertia, particle inertia, and unsteadiness are ignored. The non-dimensional parameter in the problem is the non-dimensional settling velocity Q, defined in Section 5.3.

9.1 History of the problem

The collision rate for non-interacting droplets is described in Section 5.3. To summarise, Saffman & Turner [17] showed that the collision rate increases linearly with the strain rate in turbulent flows, indicating that the same scaling should exist for pure straining flows. By contrast, when the droplet dynamics is dominated by gravity, the strain-rate is proportional to the differential settling-velocity. Between these two extreme cases, the collision rate interpolates smoothly and monotonically as a function of non-dimensional settling velocity Q.

Including hydrodynamic interactions, however, drastically changes the collision rate in the intermediate regime between strain dominated and settling dominated extremes, as shown by Dhanasekaran *et al.* [64]. The collision rate in this regime shows two important properties. First, it is no longer a monotonic function of the parameter Q. It exhibits a local maximum and a local minimum in the intermediate regime. Second, the collision rate no longer depends smoothly on Q, but shows sharp kinks at the maximum and minimum values.

Hydrodynamic interactions modify not just the collision rate but also the relative dynamics. The authors of Ref. [64] report that closed trajectories, which start and end on the collision sphere, appear for a range of values of Q. They explain that these closed trajectories give rise to the non-monotonic collision rates mentioned above. In fact, several other studies such as Batchelor

& Green [95] and Zeichner & Schowalter [96] have reported the existence of closed trajectories in relative dynamics of hydrodynamically interacting spherical particles. In particular, Ref. [96] related an observed decrease in the collision rate to appearance of closed trajectories.

However, there are several open questions. First, no quantitative theory exists which relates a decrease in collision rate to appearance of closed trajectories. Second, the sharp kinks in the collision rate as a function of Q are not understood, not even quantitatively. While the initial goal of paper D was to explain these two observations using a dynamical systems analysis similar to that performed in paper C, we could go much further and found phenomenon in the relative dynamics which was not known before. The detailed results are explained in the next Section.

9.2 Results

We explained the observed non-monotonic dependence of the collision rate on Q, seen in Fig. 2(**g**) in paper D, using bifurcation analysis. We explained the appearance of closed trajectories and showed that they cannot explain the non-monotonic dependence of the collision rate. We found that the system exhibits three qualitatively different kinds of bifurcations. First, smooth bifurcations described by usual dynamical systems theory [73] occur at $R > 2$, where R is the center-to-center distance of the droplets, dedimensionalised by the mean droplet radius $\overline{a} = (a_1 + a_2)/2$ for two droplets with radii a_1 and a_2. Second, non-smooth bifurcations occur at the boundary $R = 2$. The reason is that the mobility functions discussed in Section 4.3 are not Lipschitz continuous at the boundary, $R = 2$, not even in the continuum case $\mathrm{Kn} = 0$. Lipschitz continuity for the velocity field is assumed even in texts discussing non-smooth dynamical systems [97, 98]. No general theory describing bifurcation of non-Lipschitz continuous dynamical systems exists. Third, the existence of the boundary at $R = 2$ leads to grazing bifurcations, not observed in smooth systems [98]. These bifurcations explain the observed dependence of the collision rate on the parameter Q.

Surprisingly, we found that there exists a regime of Q where the steady-state collision rate becomes independent of Kn, even for neutral droplets. This is in contrast to the usual understanding that droplets cannot collide in the continuum approximation [10, 16, 99, 100], from which one might

conclude that the collision rate vanishes when $\mathrm{Kn} = 0$. The mechanism that causes this is similar to that discussed in paper C, described below.

We explain the mechanisms which determine collision outcomes, and how they are affected by the bifurcations described above. At very small and very large values of Q, collision outcomes are determined by grazing trajectories. These are trajectories which stretch from $R \to \infty$ to the collision sphere at $R = 2$, and are tangential to the collision sphere at the point of contact. The grazing trajectory is sensitive to the dynamics close to $R = 2$, and thus depends upon the Knudsen number. Consequently, the collision rate depends upon the Knudsen number, through the grazing trajectory.

By contrast, there is an intermediate regime, where collision outcomes are determined by a stable manifold stretching from a saddle point to $R \to \infty$. In the model considered, and for this intermediate regime, both the saddle point, and its stable manifold are far enough from the collision sphere so that they are unaffected by the effects of continuum breakdown. Then, the collision rate becomes non-zero and independent of the Knudsen number for small Kn. This is surprising, because droplets cannot collide when $\mathrm{Kn} = 0$ [10, 16, 99, 100]. From this one may be tempted to conclude that the collision rate vanishes as $\mathrm{Kn} \to 0$ [64, 65]. Our results, however, show that this is not always the case.

Spatial clustering

For the model considered, in the regime $Q > 7.88$, there are two saddle points at $R > 2$. These are labelled saddle points V and VI and are shown in Fig. 9.1. A saddle point may lead to spatial clustering in its vicinity and on its unstable manifold, if its stability exponents satisfy a certain condition. In paper D we showed this by solving the steady-state continuity equation in the vicinity of the saddle-point. Here I present a slightly different derivation. The continuity equation has the formal solution,

$$P = P_0 \exp\left(- \int_0^t \mathrm{d}s \, \boldsymbol{\nabla} \cdot \boldsymbol{V}_s \right). \tag{9.1}$$

Where the integral must be performed along particle trajectories. Near a saddle point, using $\boldsymbol{\nabla} \cdot \boldsymbol{V}_s = \lambda_+ + \lambda_-$ we find $P = P_0 \exp[-(\lambda_+ + \lambda_-)\, t]$. Consider the dynamics close to saddle point VI in Fig. 9.1 whose stable and unstable directions point along the R_1 and R_3 axis, respectively. The

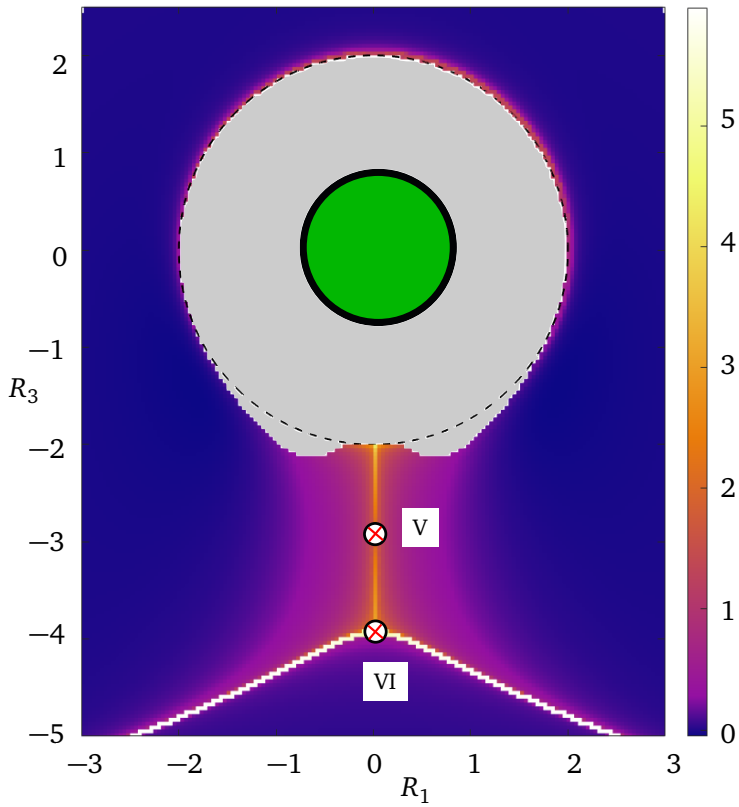

Figure 9.1: Logarithmic density of particle separations, $\log P(\boldsymbol{R})$, for $Q = 8.1$ and $a_1/a_2 = 0.9$. Encircled red crosses show saddle points V and VI. The unstable manifolds of saddle point VI show large densities. The green sphere at the center shows the smaller droplet, while the dashed circle is the collision sphere. The gray region cannot be reached by droplets approaching from afar.

separation vector from the saddle point is denoted by $(R_1, \delta R_3)$. Next we use $\delta R_3 = \delta R_3^{t=0} \exp(\lambda_- t)$ to eliminate t in Eq. (9.1) and find,

$$P \sim \delta R_3^{\left(-1-\frac{\lambda_+}{\lambda_-}\right)}. \tag{9.2}$$

In summary, P diverges algebraically with exponent $= -1 - \frac{\lambda_+}{\lambda_-}$ as $\delta R_3 \to 0$.

The above derivation allows to interpret the mechanism leading to a divergent density not just close to the saddle point but also on its unstable manifold. The reason is that the exponentially slow approach to $\delta R_3 = 0$ causes the integral in Eq. (9.1) to diverge.

10 Conclusions

The most exciting aspect of this thesis, for me, was the realisation that the collision dynamics of droplets can become independent of the Knudsen number (discussed in papers C and D), and that non-trivial fixed points can give rise to clustering (paper D). First, these results were entirely unexpected for me, after having spent the past couple of years going through the known literature on collisions of droplets in fluids. Second, the results went beyond the initial question we asked, both in scope and in applicability to models. Despite the successes in the simple models considered, the most important questions regarding these results is whether they survive a time-dependent flow and their implications for experiments, discussed in the Outlook below.

A particularly satisfying aspect of the angular dynamics of slender rods considered in paper B was the excellent agreement obtained between direct numerical simulations and theoretical predictions using a statistical model with rapidly fluctuating velocity gradients [30]. While several numerical studies before us had discussed alignment between slender rods and the Lagrangian stretching direction in homogeneous isotropic turbulence, no theory existed describing how this alignment depends upon the particle shape or on the properties of the flow near boundaries. Near the channel wall, we could obtain quantitative agreement with direct numerical simulations because the timescale of angular dynamics was much slower than the timescale of fluctuations of velocity gradients. Yet, several aspects remain unexplained, see the Outlook below.

The relation between multifractal dimensions, Eq. (6.1), gives insight into the rich mathematical structure underlying this simple model of dynamics of particles in turbulence. Both Ref. [82] which came before paper A and Ref. [84], which came after found relations similar to Eq. (6.1), at least in certain regimes. While Ref. [82] considered dynamics of particles advected in compressible flows in more than one dimension, Ref. [84] considered inertial particles in one spatial dimension. This means that the dynamics occurs in two-dimensional phase space. In those studies, the independence of $(q-1)D_q$ from q seems to occur due to rare events where large number of particles are concentrated in small volumes. This effect is captured by trajectory crossings in our simple one-dimensional toy model. Despite the mathematical successes, one must ask what the implications of these results

are for experiments. This is discussed below.

11 Outlook

Fractal dimensions in the correlated random-walk model

The relation between the fractal dimensions, Eq. (6.1) is strictly valid only when the separation between particles remains infinitesimally small. When the Lyapunov exponent is positive, this relation is satisfied only when the particles travel at small separations for long times. Fig. 5(b) in paper A suggests that in order to observe Eq. (6.1) $R \leq 10^{-6}\eta$, where η is the correlation length of the flow. This observation has important implications for the physical situation of particles in turbulent flows. Weakly inertial particles in a turbulent flow separate exponentially with a rate given by the largest Lyapunov exponent [101]. Moreover, in Nature, particles have a finite size and hydrodynamic interactions are expected to become important at particle separations of the order 10×particle radius. In typical experiments this corresponds to about 0.1×the correlation length of the flow [15, 24]. The dynamics of hydrodynamically interacting particles is the subject of paper C and paper D.

Angular dynamics of slender rods

The results obtained close to the channel boundary in paper B show quantitative agreement with DNS results. However, we analysed only the Euler angles in the flow-shear plane, ϕ. I expect that the exponent for $P(\theta)$, the distribution of the Euler angle out of the flow-shear plane can be computed using the same method. The distribution of angles near the channel center are qualitative because the analysis was performed in two dimensions for the white-noise model. While this qualitatively described the power-laws observed, it cannot predict the quantitative exponents. Such a quantitative theory would require extending the theory to three dimension.

Finally, the angular dynamics in a slowly varying fluid velocity-field, the so called persistent-flow limit [6, 102], are not understood. The persistent-flow limit is interesting because fluid flows in homogeneous isotropic turbulence exhibit Kubo numbers somewhat larger than unity [103].

Effects of interactions on droplet dynamics

The dynamical systems analysis employed in Papers C and D worked because the fluid flows in those problems are time independent. In paper D we presented a mechanism which predicts a divergent pair-correlation function, at least in the time independent case. The most important question is what are the consequences of this divergent pair-probability for experiments. Recent experiments by groups at Eindhoven University of Technology [24], and at University at Buffalo [15] show that the pair-correlation function exhibits values several orders of magnitude larger than those predicted by existing theories. These theories do not account for hydrodynamic interactions at separations of the order of a few droplet radii. The next step is to understand, first by performing numerical simulations, if this divergent pair-probability survives an average performed over fluctuating velocity-gradients.

The bifurcation analysis performed in paper D successfully explains the collision rate when the external strain and gravity are aligned with each other. The problem is degenerate due to rotational symmetry about the gravity axis. However, preliminary model simulations show that the qualitative dynamics remains the same for a small but non-zero misalignment between gravity and strain. The collision rates for this case were computed by Ref. [64]. The results show that the peak in the collision rate close to $Q = 5.67$ is replaced by a minimum close to $Q \approx 7$. How this is explained using the dynamical systems approach mentioned here is an open question.

The effect of electrical charges was considered in paper C. Water droplets in warm rain clouds are known to carry small charges, about 100 electrons for a 10 micron droplet [9]. In order to understand how these small charges affect the collision rates, it is important to account for electrical forces at close approach. Lekner [72] calculated the exact force between two conducting spheres as a function of their separation. But one must ask, do the results for conducting spheres apply to water droplets? The timescale τ_e associated to charge redistribution on a water droplet depends on the ratio of the permittivity of water, ε_w, to its electrical conductivity, σ, $\tau_e = \varepsilon_w/\sigma$ [104]. The conductivity of water is higher in the presence of ionic impurities, but even using the conductivity of pure water, it turns out that $\tau_e \approx 1.4 \times 10^{-4}$ sec. Comparing this to the particle relaxation time for relative dynamics, $\tau = \overline{a}/v_s$ for a 9 micron and a 10 micron droplet (so that the radius ratio $a_1/a_2 = 0.9$) gives, $\tau_e/\tau \approx 0.03 \ll 1$. This indicates that charge on the

droplets redistributes much faster than the droplet separation changes. Thus, we conclude that the conducting sphere approximation holds. In the future, we intend to include electrical forces described by Ref. [72] into the model considered here, and study how this affects the collision rate.

How charges affect spatial clustering of particles in turbulence is only understood for the case of small, non-hydrodynamically interacting particles with large charges [105, 106, 107]. How this clustering is modified when the charges are smaller so that hydrodynamic interactions become important is not understood. The phase space picture presented in paper C might help to understand how the pair-probability of separations behaves in the regime where both charges and hydrodynamic interactions are important. This study considered charges larger than those observed for thunderstorm droplets [9], yet smaller than those considered by previous studies [105, 106, 107]. At the charges considered, neither the saddle point nor its stable manifold passes through the non-continuum layer close to the collision sphere. At small charges, the saddle point and its stable manifold may pass close to the collision sphere causing collisions to depend upon the Knudsen number. How the transition from the Knudsen independent, large charge regime to the Knudsen dependent small charge regime occurs is an open question.

Finally, the dynamics of charged droplets in thunderstorm clouds involves background electrical fields [12]. How the distributions of relative separations of charged droplets change when a background electrical field is taken into account is not known.

ACKNOWLEDGEMENTS

I would like to start by expressing my gratitude to my supervisor Bernhard Mehlig for his unbounded enthusiasm and precise criticisms. His quest to transform every result into the most intuitive form possible has been a critical part of my PhD education. I would like to thank my co-supervisor Kristian Gustavsson for many illuminating discussions, and expert help with questions, both technical and otherwise.

I am grateful to our collaborators Zhiwen Cui and Lihao Zhao for all their work and helpful contributions. They helped me transition from the world of toy models to the realities of direct numerical simulations. I thank Reece Kearney and Greg Bewley for their perseverance, and for all the wonderful discussions.

I am grateful to the people I had the pleasure of sharing an office with: Jan, Johan, and Ludvig, for the countless interesting discussions and equally countless cups of coffees.

I thank all my friends (you know who you are) and family for their support and understanding. Finally, I am immensely thankful to Alina for her love and unending support.

Bibliography

[1] BODENSCHATZ, E, MALINOWSKI, S. P, SHAW, R. A & STRATMANN, F 2010 Can we understand clouds without turbulence? *Science* **327** (5968), 970–971.

[2] LUNDELL, F, SÖDERBERG, L. D & ALFREDSSON, P. H 2011 Fluid mechanics of papermaking. *Annual Review of Fluid Mechanics* **43** (1), 195–217.

[3] FRISCH, U 1995 *Turbulence: The Legacy of A. N. Kolmogorov*. Cambridge University Press.

[4] OTT, E 2002 *Chaos in Dynamical Systems*, 2nd edn. Cambridge University Press.

[5] CENCINI, M, CECCONI, F & VULPIANI, A 2009 *Chaos: From simple models to Complex Systems*. WORLD SCIENTIFIC.

[6] GUSTAVSSON, K & MEHLIG, B 2016 Statistical models for spatial patterns of heavy particles in turbulence. *Advances in Physics* **65** (1), 1–57.

[7] WILKINSON, M, MEHLIG, B & BEZUGLYY, V 2006 Caustic activation of rain showers. *Phys. Rev. Lett.* **97**, 048501.

[8] SUNDARAM, S & COLLINS, L. R 1997 Collision statistics in an isotropic particle-laden turbulent suspension. Part 1. Direct numerical simulations. *Journal of Fluid Mechanics* **335**, 75–109.

[9] TAKAHASHI, T 1973 Measurement of electric charge of cloud droplets, drizzle, and raindrops. *Reviews of Geophysics* **11** (4), 903–924.

[10] PRUPPACHER, H. R & KLETT, J. D 2010 *Microphysics of Clouds and Precipitation*. Springer Netherlands.

[11] KIM, S & KARRILA, S. J 1991 *Microhydrodynamics*. Butterworth-Heinemann.

[12] HARRISON, R. G, NICOLL, K. A & AMBAUM, M. H. P 2015 On the microphysical effects of observed cloud edge charging. *Quarterly Journal of the Royal Meteorological Society* **141** (692), 2690–2699.

[13] GRABOWSKI, W. W & WANG, L.-P 2013 Growth of Cloud Droplets in a Turbulent Environment. *Annual Review of Fluid Mechanics* **45** (1), 293–324.

[14] HAPPEL, J & BRENNER, H 1983 *Low Reynolds number hydrodynamics*. Springer, Dordrecht.

[15] BRAGG, A. D, HAMMOND, A. L, DHARIWAL, R & MENG, H 2022 Hydrodynamic interactions and extreme particle clustering in turbulence. *Journal of Fluid Mechanics* **933**, A31.

[16] PUMIR, A & WILKINSON, M 2016 Collisional aggregation due to turbulence. *Annual Review of Condensed Matter Physics* **7** (1), 141–170.

[17] SAFFMAN, P. G & TURNER, J. S 1956 On the collision of drops in turbulent clouds. *Journal of Fluid Mechanics* **1** (1), 16–30.

[18] MAXEY, M. R 1987 The gravitational settling of aerosol particles in homogeneous turbulence and random flow fields. *Journal of Fluid Mechanics* **174**, 441–465.

[19] BEC, J 2003 Fractal clustering of inertial particles in random flows. *Physics of Fluids* **15** (11), L81–L84.

[20] WILKINSON, M, MEHLIG, B, ÖSTLUND, S & DUNCAN, K. P 2007 Unmixing in random flows. *Physics of Fluids* **19** (11), 113303.

[21] SOMMERER, J. C & OTT, E 1993 Particles Floating on a Moving Fluid: A Dynamically Comprehensible Physical Fractal. *Science* **259** (5093), 335–339.

[22] BEC, J 2005 Multifractal concentrations of inertial particles in smooth random flows. *Journal of Fluid Mechanics* **528**, 255–277.

[23] HARTE, D 2001 *Multifractals: theory and applications*. Chapman and Hall/CRC; 1 edition (June 26, 2001).

[24] YAVUZ, M, KUNNEN, R, VAN HEIJST, G & CLERCX, H 2018 Extreme small-scale clustering of droplets in turbulence driven by hydrodynamic interactions. *Phys. Rev. Lett.* **120**, 244504.

[25] TENNETI, S & SUBRAMANIAM, S 2014 Particle-Resolved Direct Numerical Simulation for Gas-Solid Flow Model Development. *Annual Review of Fluid Mechanics* **46** (1), 199–230.

[26] JEFFREY, D. J & ONISHI, Y 1984 Calculation of the resistance and mobility functions for two unequal rigid spheres in low-Reynolds-number flow. *Journal of Fluid Mechanics* **139**, 261–290.

[27] SCHLAMP, R. J, GROVER, S. N, PRUPPACHER, H. R & HAMIELEC, A. E 1979 A Numerical Investigation of the Effect of Electric Charges and Vertical External Electric Fields an the Collision Efficiency of Cloud Drops: Part II. *Journal of the Atmospheric Sciences* **36** (2), 339–349.

[28] ATKINSON, W. R & PALUCH, I 1968 Analytical approximation of numerically determined collision efficiencies of hydrometeors. *Journal of Geophysical Research* **73** (6), 2035–2048.

[29] PALUCH, I. R 1970 Theoretical collision efficiencies of charged cloud droplets. *Journal of Geophysical Research (1896-1977)* **75** (9), 1633–1640.

[30] ZHAO, L, GUSTAVSSON, K, NI, R, KRAMEL, S, VOTH, G. A, ANDERSSON, H. I & MEHLIG, B 2019 Passive directors in turbulence. *Phys. Rev. Fluids* **4**, 054602.

[31] TOSCHI, F & BODENSCHATZ, E 2009 Lagrangian properties of particles in turbulence. *Annual Review of Fluid Mechanics* **41**, 375–404.

[32] RISKEN, H 1986 *The Fokker-Planck Equation: Methods of Solution and Applications*. Springer, Berlin, Heidelberg.

[33] WILKINSON, M, BEZUGLYY, V & MEHLIG, B 2009 Fingerprints of random flows? *Physics of Fluids* **21** (4), 43304.

[34] PARSA, S, GUASTO, J. S, KISHORE, M, OUELLETTE, N. T, GOLLUB, J. P & VOTH, G. A 2011 Rotation and alignment of rods in two-dimensional chaotic flow. *Physics of Fluids* **23** (4), 43302.

[35] ISHIHARA, T, KANEDA, Y, YOKOKAWA, M, ITAKURA, K & UNO, A 2007 Small-scale statistics in high-resolution direct numerical simulation

of turbulence: Reynolds number dependence of one-point velocity gradient statistics. *Journal of Fluid Mechanics* **592**, 335–366.

[36] STRANG, G 2009 *Introduction to Linear Algebra*, 4th edn. Wellesley-Cambridge Press.

[37] KOLMOGOROV, A. N, LEVIN, V, HUNT, J. C. R, PHILLIPS, O. M & WILLIAMS, D 1991 The local structure of turbulence in incompressible viscous fluid for very large reynolds numbers. *Proceedings of the Royal Society of London. Series A: Mathematical and Physical Sciences* **434** (1890), 9–13.

[38] PUMIR, A & WILKINSON, M 2011 Orientation statistics of small particles in turbulence. *New Journal of Physics* **13** (9), 093030.

[39] SHEN, X & WARHAFT, Z 2000 The anisotropy of the small scale structure in high reynolds number ($r_\lambda \sim 1000$) turbulent shear flow. *Physics of Fluids* **12** (11), 2976–2989.

[40] POPE, S. B 2000 *Turbulent Flows*. Cambridge University Press.

[41] MOIN, P & KIM, J 1982 Numerical investigation of turbulent channel flow. *Journal of Fluid Mechanics* **118**, 341–377.

[42] TOSCHI, F, AMATI, G, SUCCI, S, BENZI, R & PIVA, R 1999 Intermittency and structure functions in channel flow turbulence. *Phys. Rev. Lett.* **82**, 5044–5047.

[43] KOBAYASHI, H, MATSUMOTO, E, FUKUSHIMA, N, TANAHASHI, M & MIYAUCHI, T 2011 Statistical properties of the local structure of homogeneous isotropic turbulence and turbulent channel flows. *Journal of Turbulence* **12**, N12.

[44] PUMIR, A 2017 Structure of the velocity gradient tensor in turbulent shear flows. *Phys. Rev. Fluids* **2**, 074602.

[45] GUSTAVSSON, K, EINARSSON, J & MEHLIG, B 2014 Tumbling of small axisymmetric particles in random and turbulent flows. *Phys. Rev. Lett.* **112**, 014501.

[46] VREMAN, A. W & KUERTEN, J. G. M 2014 Statistics of spatial derivatives of velocity and pressure in turbulent channel flow. *Physics of Fluids* **26** (8), 085103.

[47] WILKINSON, M & MEHLIG, B 2005 Caustics in turbulent aerosols. *Europhysics Letters (EPL)* **71** (2), 186–192.

[48] MEHLIG, B, WILKINSON, M, DUNCAN, K, WEBER, T & LJUNGGREN, M 2005 Aggregation of inertial particles in random flows. *Phys. Rev. E* **72**, 051104.

[49] DUNCAN, K, MEHLIG, B, ÖSTLUND, S & WILKINSON, M 2005 Clustering by mixing flows. *Phys. Rev. Lett.* **95**, 240602.

[50] SCHUMACHER, J, SCHEEL, J. D, KRASNOV, D, DONZIS, D. A, YAKHOT, V & SREENIVASAN, K. R 2014 Small-scale universality in fluid turbulence. *Proceedings of the National Academy of Sciences* **111** (30), 10961–10965.

[51] GUSTAVSSON, K 2009 Advective collisions in random flows. Licentiate thesis, Göteborgs universitet.

[52] GUSTAVSSON, K, JUCHA, J, NASO, A, LÉVÊQUE, E, PUMIR, A & MEHLIG, B 2017 Statistical model for the orientation of nonspherical particles settling in turbulence. *Phys. Rev. Lett.* **119**, 254501.

[53] BORGNINO, M, GUSTAVSSON, K, DE LILLO, F, BOFFETTA, G, CENCINI, M & MEHLIG, B 2019 Alignment of nonspherical active particles in chaotic flows. *Phys. Rev. Lett.* **123**, 138003.

[54] BATCHELOR, G. K 2000 *An Introduction to Fluid Dynamics*. Cambridge University Press.

[55] CANDELIER, F & MEHLIG, B 2016 Settling of an asymmetric dumbbell in a quiescent fluid. *Journal of Fluid Mechanics* **802**, 174–185.

[56] LOVALENTI, P & BRADY, J 1993 The force on a bubble, drop or particle in arbitrary time-dependent motion at small Reynolds number. *Phys. Fluids* **5**, 2104–2116.

[57] PIKOVSKY, A. S 1992 Statistics of trajectory separation in noisy dynamical systems. *Phys. Lett. A* **165**, 33.

[58] DEUTSCH, J. M 1984 Noise-induced phases of iterated functions. *Phys. Rev. Lett.* **52**, 1230–1233.

[59] DEUTSCH, J. M 1985 Aggregation-disorder transition induced by fluctuating random forces. *Journal of Physics A: Mathematical and General* **18** (9), 1449–1456.

[60] WILKINSON, M & MEHLIG, B 2003 Path coalescence transition and its applications. *Phys. Rev. E* **68**, 040101.

[61] WILKINSON, M, MEHLIG, B, GUSTAVSSON, K & WERNER, E 2012 Clustering of exponentially separating trajectories. *Eur. Phys. J. B* **85**, 18.

[62] DUBEY, A 2020 Separations and relative angles of particles in turbulence. Licentiate thesis, Göteborgs universitet.

[63] JEFFERY, G. B 1922 The motion of ellipsoidal particles immersed in a viscous fluid. *Proceedings of the Royal Society of London Series A* **102** (715), 161–179.

[64] DHANASEKARAN, J, ROY, A & KOCH, D. L 2021 Collision rate of bidisperse spheres settling in a compressional non-continuum gas flow. *Journal of Fluid Mechanics* **910**, A10.

[65] DHANASEKARAN, J, ROY, A & KOCH, D. L 2021 Collision rate of bidisperse, hydrodynamically interacting spheres settling in a turbulent flow. *Journal of Fluid Mechanics* **912**, A5.

[66] JEFFREY, D. J 1992 The calculation of the low Reynolds number resistance functions for two unequal spheres. *Physics of Fluids A* **4** (1), 16–29.

[67] O'NEILL, M. E & MAJUMDAR, R 1970 Asymmetrical slow viscous fluid motions caused by the translation or rotation of two spheres. Part I: The determination of exact solutions for any values of the ratio of radii and separation parameters. *Zeitschrift für angewandte Mathematik und Physik ZAMP* **21** (2), 164–179.

[68] WANG, H, ZINCHENKO, A. Z & DAVIS, R. H 1994 The Collision Rate of Small Drops in Linear Flow Fields. *Journal of Fluid Mechanics* **265**, 161–188.

[69] SUNDARARAJAKUMAR, R. R & KOCH, D. L 1996 Non-continuum lubrication flows between particles colliding in a gas. *Journal of Fluid Mechanics* **313**, 283–308.

[70] KLETT, J. D & DAVIS, M 1973 Theoretical collision efficiencies of cloud droplets at small Reynolds numbers. *Journal of the Atmospheric Sciences* **30** (1), 107–117.

[71] ARDEKANI, A. M & RANGEL, R. H 2006 Unsteady motion of two solid spheres in Stokes flow. *Physics of Fluids* **18** (10), 1–14.

[72] LEKNER, J 2012 Electrostatics of two charged conducting spheres. *Proceedings of the Royal Society A: Mathematical, Physical and Engineering Sciences* **468** (2145), 2829–2848.

[73] STROGATZ, S 2000 *Nonlinear Dynamics and Chaos: With Applications to Physics, Biology, Chemistry and Engineering*. Westview.

[74] HENTSCHEL, H. G & PROCACCIA, I 1983 The infinite number of generalized dimensions of fractals and strange attractors. *Physica D: Nonlinear Phenomena* **8** (3), 435–444.

[75] GRASSBERGER, P & PROCACCIA, I 1983 Generalized dimensions of strange attractors. *Physical Review Letters* **97A**, 227–230.

[76] BEC, J, BIFERALE, L, CENCINI, M, LANOTTE, A, MUSACCHIO, S & TOSCHI, F 2007 Heavy particle concentration in turbulence at dissipative and inertial scales. *Phys. Rev. Lett.* **98**, 084502.

[77] WILKINSON, M, MEHLIG, B & GUSTAVSSON, K 2010 Correlation dimension of inertial particles in random flows. *EPL (Europhysics Letters)* **89** (5), 50002.

[78] DEVENISH, B. J, BARTELLO, P, BRENGUIER, J. L, COLLINS, L. R, GRABOWSKI, W. W, IJZERMANS, R. H, MALINOWSKI, S. P, REEKS, M. W, VASSILICOS, J. C, WANG, L. P & WARHAFT, Z 2012 Droplet growth in

warm turbulent clouds. *Quarterly Journal of the Royal Meteorological Society* **138** (667), 1401–1429.

[79] VON SMOLUCHOWSKI, M 1917 Mathematical theory of the kinetics of the coagulation of colloidal solutions. *Z. Phys. Chem* **92** (129), 129–68.

[80] FESSLER, J. R, KULICK, J. D & EATON, J. K 1994 Preferential concentration of heavy particles in a turbulent channel flow. *Physics of Fluids* **6** (11), 3742–3749.

[81] MEHLIG, B & WILKINSON, M 2004 Coagulation by random velocity fields as a kramers problem. *Phys. Rev. Lett.* **92**, 250602.

[82] BEC, J, GAWEDZKI, K & HORVAI, P 2004 Multifractal clustering in compressible flows. *Phys. Rev. Lett.* **92**, 224501.

[83] MEIBOHM, J, PISTONE, L, GUSTAVSSON, K & MEHLIG, B 2017 Relative velocities in bidisperse turbulent suspensions. *Phys. Rev. E* **96**, 061102.

[84] MEIBOHM, J, GUSTAVSSON, K, BEC, J & MEHLIG, B 2020 Fractal catastrophes. *New Journal of Physics* **22** (1), 13033.

[85] ZHAO, L & ANDERSSON, H. I 2016 Why spheroids orient preferentially in near-wall turbulence. *Journal of Fluid Mechanics* **807**, 221–234.

[86] NI, R, OUELETTE, N. T & VOTH, G. A 2014 Alignment of vorticity and rods with La83ngian fluid stretching in turbulence. *J. Fluid Mech.* **743**, R3.

[87] BALKOVSKY, E & FOUXON, A 1999 Universal long-time properties of lagrangian statistics in the batchelor regime and their application to the passive scalar problem. *Phys. Rev. E* **60**, 4164–4174.

[88] CHERTKOV, M, KOLOKOLOV, I, LEBEDEV, V & TURITSYN, K 2005 Polymer statistics in a random flow with mean shear. *Journal of Fluid Mechanics* **531**, 251–260.

[89] CUI, Z 2020 Private communication .

[90] WANG, L. P, AYALA, O, KASPRZAK, S. E & GRABOWSKI, W. W 2005 Theoretical formulation of collision rate and collision efficiency of

hydrodynamically interacting cloud droplets in turbulent atmosphere. *Journal of the Atmospheric Sciences* **62** (7 II), 2433–2450.

[91] POINCARÉ, H 1890 Sur le problème des trois corps et les équations de dynamique. *Acta Mathematica* **13**, 1–270.

[92] POINCARÉ, H 1899 *Méthodes nouvelles de la mécanique céleste*. Gauthier-Villars et fils.

[93] MURRAY, J. D 2001 *Mathematical biology II: spatial models and biomedical applications*. Springer New York.

[94] MURRAY, J. D 2001 *Mathematical biology I: An Introduction*. Springer New York.

[95] BATCHELOR, G. K & GREEN, J. T 1972 The hydrodynamic interaction of two small freely-moving spheres in a linear flow field. *Journal of Fluid Mechanics* **56** (2), 375–400.

[96] ZEICHNER, G. R & SCHOWALTER, W. R 1977 Use of trajectory analysis to study stability of colloidal dispersions in flow fields. *AIChE Journal* **23** (3), 243–254.

[97] BROGLIATO, B 2016 *Nonsmooth Mechanics*. Springer, Cham.

[98] DI BERNARDO LAUREA, M, CHAMPNEYS, A. R, BUDD, C. J & KOWALCZYK, P 2008 *Piecewise-smooth Dynamical Systems*. Springer London.

[99] DAVIS, R. H 1984 The rate of coagulation of a dilute polydisperse system of sedimenting spheres. *Journal of Fluid Mechanics* **145**, 179–199.

[100] HOCKING, L. M 1973 The effect of slip on the motion of a sphere close to a wall and of two adjacent spheres. *Journal of Engineering Mathematics* **7** (3), 207–221.

[101] BEC, J, BIFERALE, L, BOFFETTA, G, CENCINI, M, MUSACCHIO, S & TOSCHI, F 2006 Lyapunov exponents of heavy particles in turbulence. *Physics of Fluids* **18** (9).

[102] MEIBOHM, J & MEHLIG, B 2019 Heavy particles in a persistent random flow with traps. *Phys. Rev. E* **100**, 023102.

[103] GIRIMAJI, S. S & POPE, S. B 1990 A diffusion model for velocity gradients in turbulence. *Physics of Fluids A: Fluid Dynamics* **2** (2), 242–256.

[104] HAUS, H. A & MELCHER, J. R 1989 *Electromagnetic Fields and Energy*. Prentice-Hall.

[105] LU, J, NORDSIEK, H, SAW, E. W & SHAW, R. A 2010 Clustering of charged inertial particles in turbulence. *Phys. Rev. Lett.* **104**, 184505.

[106] LU, J, NORDSIEK, H & SHAW, R. A 2010 Clustering of settling charged particles in turbulence: theory and experiments. *New Journal of Physics* **12** (12), 123030.

[107] LU, J & SHAW, R. A 2015 Charged particle dynamics in turbulence: Theory and direct numerical simulations. *Physics of Fluids* **27** (6), 065111.

PART IV
APPENDIX

A Exit times

Let a stochastic process x satisfy the Fokker-Planck equation,

$$\frac{\partial P}{\partial t} = \mathscr{L}_{\mathrm{FP}} P \; ; \; P(x,0|x_0,0) = \delta(x-x_0), \tag{A.1}$$

$$P(x,t|x_0,0) = 0 \text{ if } x \in \delta\Omega. \tag{A.2}$$

So that we impose absorbing boundary conditions on the boundary $\delta\Omega$ of the domain Ω. The probability that x has not reached the boundary $\delta\Omega$ at time t is given by $\int_\Omega dx P(x,t|x_0,0)$, so that the cumulative distribution function for the exit time $\rho(t)$ reads,

$$\rho(t) = \frac{\partial}{\partial t}(1 - \int_\Omega \mathrm{d}x P(x,t|x_0,0)), \tag{A.3}$$

$$= -\int_\Omega \mathrm{d}x \frac{\partial}{\partial t} P(x,t|x_0,0) \tag{A.4}$$

The n—th moment of the first exit time, $T_n(x_0)$ can be written,

$$T_n(x_0) = \int_0^\infty \mathrm{d}t \; t^n \rho(t), \tag{A.5}$$

$$= \int_0^\infty \mathrm{d}t \; t^n \rho(t), \tag{A.6}$$

$$= \int_\Omega \mathrm{d}x p_n(x,x_0) \tag{A.7}$$

where $p_n(x,x_0) = -\int_0^\infty \mathrm{d}t \; t^n \frac{\partial}{\partial t} P(x,t|x_0,0)$. From applying the Fokker-Planck operator to this expression one obtains the hierarchy of equations,

$$\mathscr{L}_{\mathrm{FP}}(x)p_1(x,x_0) = -\delta(x-x_0), \tag{A.8}$$
$$\mathscr{L}_{\mathrm{FP}}(x)p_2(x,x_0) = -p_1(x,x_0), \tag{A.9}$$
$$\mathscr{L}_{\mathrm{FP}}(x)p_3(x,x_0) = -p_2(x,x_0), \tag{A.10}$$
$$\cdots$$

here $p_n(x,x_0)$ satisfy the same boundary conditions as the transition probability $P(x,t|x_0,0)$.

A.1 Mean tumbling time asymptotics

We start with the integral expression, Eq.(A17) in Appendix A, paper A,

$$T_1 = \frac{\sqrt{\pi}12^{\frac{1}{6}}}{D}\left(\frac{D}{s\Lambda}\right)^{\frac{2}{3}}\int_0^\infty \mathrm{d}y\ \frac{1}{\sqrt{y}}e^{-\left(\frac{3}{2}\right)^{\frac{1}{3}}\left(\frac{s}{D}\right)^{\frac{2}{3}}\frac{\delta\Lambda}{\Lambda^{1/3}}y-y^3}. \tag{A.11}$$

Small $\delta\Lambda$ asymptotics

First we change notation to simplify the expressions. Denote,

$$c = \frac{\sqrt{\pi}12^{\frac{1}{6}}}{D}\left(\frac{D}{s\Lambda}\right)^{\frac{2}{3}} \tag{A.12}$$
$$d = \left(\tfrac{3}{2}\right)^{\frac{1}{3}}\left(\tfrac{s}{D}\right)^{\frac{2}{3}}\frac{1}{\Lambda^{1/3}}, \tag{A.13}$$

so that Eq. (A.11) reads,

$$T_1 = c\int_0^\infty \mathrm{d}y\ \frac{1}{\sqrt{y}}e^{-d\delta\Lambda y-y^3}. \tag{A.14}$$

Now $\delta\Lambda \ll \left(\frac{D}{s}\right)^{\frac{2}{3}}$, coresponds to $d\delta\Lambda \ll 1$. Thus we Taylor expand $e^{-d\delta\Lambda y}$ to obtain,

$$T_1 = c \int_0^\infty \mathrm{d}y \; \frac{1}{\sqrt{y}} e^{-y^3} \sum_{n=0}^{\infty} \frac{(-d\delta\Lambda)^n}{n!} y^n, \tag{A.15}$$

$$= c \sum_{n=0}^{\infty} \frac{(-d\delta\Lambda)^n}{n!} \int_0^\infty \mathrm{d}y \; y^{n-\frac{1}{2}} e^{-y^3} \tag{A.16}$$

$$= c \sum_{n=0}^{\infty} \frac{(-d\delta\Lambda)^n}{n!} \frac{1}{3} \Gamma\left(\frac{2n+1}{6}\right) \tag{A.17}$$

Part V
Research papers

Paper A

https://doi.org/10.1103/PhysRevE.98.062117

Paper B

https://doi.org/10.1017/jfm.2020.547

Paper C

https://arxiv.org/abs/2106.11543

Paper D